Baarlink, C., Plessner, M., Sherrard, A., Morita, K., Misu, S., Virant, D., ... Robert Grosse, R. (2017). A transient pool of nuclear F-actin at mitotic exit controls chromatin organization. *Nature Cell Biology*, *19*(12), 1389-1399. https://doi.org/10.1038/ncb3641

A transient pool of nuclear F-actin at mitotic exit controls chromatin organization.

Christian Baarlink[1#], Matthias Plessner[1#], Alice Sherrard[2#], Kohtaro Morita[3], Shinji Misu[3], David Virant[4], Eva-Maria Kleinschnitz[1], Robert Harniman[5], Dominic Alibhai[6], Stefan Baumeister[7], Kei Miyamoto[3], Ulrike Endesfelder[4], Abderrahmane Kaidi[2], and Robert Grosse[1]

[1]Institute of Pharmacology, BPC Marburg, University of Marburg, Karl-von-Frisch-Str. 1, 35043 Marburg, Germany

[2]School of Cellular and Molecular Medicine, Biomedical Sciences, University of Bristol, University Walk, Bristol BS8 1TD, United Kingdom

[3]Faculty of Biology-Oriented Science and Technology, Kindai University, 930 Nishimitani, Wakayama 649-6493, Japan

[4]Department of Systems and Synthetic Microbiology, Max Planck Institute for Terrestrial Microbiology and LOEWE Center for Synthetic Microbiology (SYNMIKRO), Karl-von-Frisch-Str. 16, 35043 Marburg, Germany

[5]Electron Microscopy Unit, School of Chemistry, Biomedical Sciences, University of Bristol, Bristol BS8 1TS, United Kingdom

[6] Wolfson Bioimaging Facility, University of Bristol, Bristol BS8 1TD, United Kingdom

[7]Protein Analytics, Faculty of Biology, University of Marburg, Karl-von-Frisch-Str. 8, 35043 Marburg, Germany

[#]These authors contributed equally.

Reestablishment of nuclear structure and chromatin organization after cell division is integral for genome regulation or development and is frequently altered during cancer progression. The mechanisms underlying chromatin expansion in daughter cells remain largely unclear. Here, we describe the transient formation of nuclear actin filaments (F-actin) during mitotic exit. These nuclear F-actin structures assemble in daughter cell nuclei and undergo dynamic reorganization to promote nuclear protrusions and volume expansion throughout early G_1 of the cell cycle. Specific inhibition of this nuclear F-actin assembly impaired nuclear expansion and chromatin decondensation after mitosis and during early mouse embryonic development. Biochemical screening for mitotic nuclear F-actin interactors identified the actin-disassembling factor Cofilin-1. Optogenetic regulation of Cofilin-1 revealed its critical role for controlling timing, turnover and dynamics of F-actin assembly inside daughter cell nuclei. Our findings identify a cell cycle-specific and spatiotemporally controlled form of nuclear F-actin that reorganizes the mammalian nucleus after mitosis.

Introduction

Cytoplasmic actin polymerization at plasma membranes is an essential and versatile process that defines cellular shape, determines cell polarity, cell-cell and cell-matrix interactions, and drives cytokinesis [1]. In addition, it is well established that actin resides in the nuclear compartment of somatic cells [2,3]. For example, monomeric actin is stably assembled into

chromatin remodeling complexes [4,5], while a dynamic pool of actin appears to constantly shuttle between the nucleus and cytoplasm in an Importin 9- and Exportin 6-dependent manner [6]. Similarly, many actin-regulatory proteins have been described to enter the nuclear compartment [2]. More recently, using nuclear-targeted probes, the presence of F-actin structures was demonstrated in mammalian cell nuclei in response to serum, integrin signaling or DNA damage [7–9]. However, whether transient and dynamic nuclear actin filaments exert fundamental structural functions in somatic cells to spatially reorganize nuclear architecture has not been investigated [10].

Mitotic cell division relies on a complex cascade of mechanistic processes to precisely ensure maintenance of genomic organization and integrity in the emerging daughter cells. During mitotic exit, newly formed cells undergo a profound reorganization of their nuclear content to reestablish an interphase nucleus, which is accompanied by a striking expansion in nuclear size and volume [11,12]. Further key processes include the reformation of a nuclear envelope and lamina, assembly of nuclear pore complexes, and decondensation as well as reorganization of the highly condensed mitotic chromosomes [13,14]. Surprisingly, the cellular mechanisms, which drive nuclear expansion while reversing mitotic chromosomes into an interphase chromatin state, remain largely unexplored [11,15,16].

RESULTS

Transient nuclear F-actin assembly during mitotic exit

We recently reported an approach to monitor endogenous nuclear F-actin dynamics without detectable effects on nucleocytoplasmic shuttling or the polymerization state of actin[8]. Our live-cell compatible approach relies on a transiently binding nanobody directed against actin fused to a nuclear localization signal (anti-Actin-Chromobody-GFP-NLS), herein referred to as nAC-GFP (nuclear Actin-Chromobody-GFP) [8]. While examining mouse fibroblasts stably expressing nAC-GFP together with LifeAct-mCherry to co-visualize cytoplasmic actin, we observed the striking and transient appearance of nuclear actin filament structures when daughter cell nuclei formed (Fig. 1a and Supplementary Video 1). These actin filaments were constantly and dynamically reorganized within the nuclear compartment (as visualized by a nanobody against Lamin A/C), arguing for a spatiotemporal function during the final stages of cell division (Fig. 1b and Supplementary Video 2). Of note, nuclear actin concentrations appeared to be constant during exit from mitosis and were not affected by the presence of nAC (Supplementary Fig. 1a, b).

Cell cycle-associated nuclear actin filaments could be detected and quantified using nAC-GFP or a shuttling Actin-Chromobody (sAC) with comparable frequencies (Fig. 1c, 3a and Supplementary Video 3). Transient nuclear actin polymerization persisted for 60-70 minutes during early G_1 phase, followed by filament disassembly upon further progression into interphase (Fig. 1d and Supplementary Video 1). Importantly, we confirmed our observations by using the F-actin marker phalloidin in fixed, but otherwise native, untreated cells (Fig. 1e). Nuclear actin polymerization at mitotic exit could also be observed in MCF10A breast epithelial, RPE-1 retinal pigmented epithelial as well as HT1080 fibrosarcoma cells, arguing for a conserved feature among mammalian cell types (Supplementary Fig. 1c-e).

Mitotic nuclear actin filaments were not affected by silencing of the nucleoskeletal proteins Emerin or Lamin A/C (Supplementary Fig. 1f-h), or expression of a dominant-negative KASH (Klarsicht/ANC-1/Syne-1 homology) domain (Supplementary Fig. 1i), shown to disrupt the LINC (Linker of Nucleoskeleton and Cytoskeleton) complex [17], suggesting that these filaments are different in origin and function from those forming upon cell spreading and integrin-dependent signaling [8].

Analysis of nuclear F-actin at mitotic exit using super-resolution microscopy

Next, cells stably expressing nAC fused to the photoconvertible fluorescent protein Dendra2 were imaged by PALM (Fig. 2a and Supplementary Fig. 2a). Under these conditions, 96% of all cells showed nuclear actin filaments at mitotic exit. Actin filaments were of several micrometer lengths with an apparent width of about 50-90 nm, which can be explained by single actin fibers stained with nAC-Dendra2 of about 10 nm width and thin bundles of about 2-5 fiber diameters convolved with the achieved PALM resolution of about 40 nm (Fig. 2b and Supplementary Fig. 2a, b).

To further investigate native cells, phalloidin staining was performed to confirm these findings using STORM imaging on cells fixed at defined time points during mitotic exit (Supplementary Fig. 2c). This revealed nuclear actin fibers for up to 60 minutes after anaphase. The reduced background and improved resolution of 30 nm allowed us to detect a population of even thinner, 40 nm wide nuclear actin filaments in addition to thicker, more bundled subsets of F-actin structures (Fig. 2c, d and Supplementary Fig. 2c).

104

105 **Postmitotic nuclear volume expansion requires nuclear actin polymerization**

106 To gain insight into the functional role of nuclear F-actin formation in early G_1, we visualized
107 nuclear actin filaments together with a fluorescently-labeled histone H2B to label the nuclear
108 compartment. This revealed a substantial expansion of nuclear volume during the period of
109 nuclear F-actin assembly as well as distinct nuclear protrusions associated with the emerging
110 dynamic nuclear F-actin structures (Fig. 3a and Supplementary Video 4).

111 To assess a potential role of nuclear F-actin formation in reshaping the newly forming
112 nuclei after cell division, we first tested for the effects of various pharmacological inhibitors of
113 the actin cytoskeleton that were directly added under the microscope to cells exiting mitosis.
114 The actin-depolymerizing agents Cytochalasin D or Latrunculin B robustly impaired nuclear
115 volume expansion, while the Arp2/3 inhibitor CK-666 had no effect (Supplementary Fig. 3a, b).

116 As pharmacological agents interfere globally with actin dynamics, we aimed to directly
117 assess the impact of nuclear actin by expression of its specific nuclear export factor Exportin 6
118 to enhance nuclear export of actin monomers (Supplementary Fig. 1b) [15]. This not only resulted
119 in a strongly reduced number of cells displaying nuclear F-actin during mitotic exit (Fig. 3b), but
120 also in a significantly impaired volume expansion of daughter nuclei (Fig. 3c, d).

121 To more specifically address the role of polymerized nuclear actin, we generated cell
122 lines stably expressing a doxycycline-inducible, nuclear-targeted version of the polymerization-
123 deficient actin mutant actin^{R62D} (NLS-BFP-actin^{R62D}) [8,18], to dilute the amount of polymerization-
124 competent actin monomers within the nuclear compartment. Similar to expression of Exportin

6, this approach resulted in a strong reduction of nuclear actin filaments as well as impaired nuclear expansion compared to control cells expressing BFP-NLS only (Fig. 3e-g). To control for any effects potentially arising from an increased concentration of nuclear actin monomers, we additionally compared the effects of actin^{R62D} to wild-type actin (actin^{wt}) instead of BFP. Given the potential limitations of fluorophore-tagged actin[19], we generated doxycycline-inducible Flag-NLS-actin constructs fused to a self-cleavable SNAP-tag, which allowed us to indirectly identify expression of these Flag-actin derivatives in live dividing cells (Supplementary Fig. 3c-f). Importantly, this experimental setup confirmed our results (Fig. 3g); clearly demonstrating the critical need of a polymerization-competent pool of nuclear actin required for nuclear volume expansion.

Noteworthy, the effects of nuclear F-actin on nuclear volume expansion were specific for cells at the mitotic exit, as no differences in nuclear volume could be detected among nuclei of cells arrested in interphase during induction of actin^{R62D} expression (Supplementary Fig. 3g). Furthermore, global transcriptional inhibition by the CDK inhibitory drug Flavopiridol during cell division did not affect the rate of daughter nuclei expansion (Supplementary Fig. 3h, i), excluding altered transcription as a cause of the observed phenotype.

Using atomic force microscopy (AFM) on isolated nuclei from synchronized live cells enabled us to visualize the structure of the nuclear surface in early G_1 as well as interphase (Fig. 3h). This revealed a remarkably rough nuclear surface indicative of nuclear protrusions in postmitotic control cells expressing Flag-NLS-actin^{wt}, which were absent in Flag-NLS-actin^{R62D} expressing nuclei displaying an overall much flatter nuclear surface (Fig. 3h, i). Similar nuclear protrusions were observed on postmitotic nuclei from untransfected cells. Of note, induction of

chromatin decompaction by Trichostatin A (TSA)-treatment of interphase nuclei [20] did not result in an increased nuclear surface roughness (Fig. 3h, j), arguing for a cell cycle-specific phenomenon that critically depends on the involvement of nuclear F-actin formation in early G_1.

Nuclear actin assembly affects early G_1 chromatin reorganization

While visualizing nuclear actin dynamics together with the histone H2B, we found nuclear F-actin to reside within interchromatin spaces in the emerging daughter cell nuclei (Fig. 4a, Supplementary Video 3). This observation as well as the time period of nuclear actin polymerization during which chromatin decondensation takes place [12], prompted us to further investigate a potential role for F-actin in this process.

Quantifications of chromatin density assessed by 3D H2B-mCherry fluorescence intensities revealed a significantly higher degree of chromatin compaction in postmitotic nuclei impaired for the assembly of nuclear F-actin either by expression of Exportin 6 or nuclear-targeted actin^{R62D} (Fig. 4b-e).

To more directly measure the degree of chromatin compaction, we established a fluorescent lifetime imaging microscopy (FLIM) assay to determine fluorescence energy transfer (FRET) between GFP- and mCherry-tagged histone H2B (Supplementary Fig. 4a, b) [21]. Consistent with a role of nuclear F-actin in postmitotic chromatin dynamics, we found that induced expression of Flag-NLS-actin^{R62D} but not Flag-NLS-actin^{wt} (Fig. 4f, g), as well as expression of

167 Exportin 6 (Fig. 4h, i) resulted in a significantly reduced fluorescence lifetime of GFP-H2B in
168 synchronized early G_1 cells (Fig. 4f-i).

169 Given the conserved roles of increased histone H3 Ser-10 phosphorylation (H3S10ph)
170 and decreased histone H4 Lys-16 acetylation (H4K16ac) in mitotic chromatin condensation [22],
171 we confirmed the effects of altered nuclear F-actin assembly on chromatin reorganization by
172 analyzing these histone modifications in cells synchronized by mitotic shake-off. While control
173 cells (BFP-NLS) reestablished lower levels of H3S10ph and higher levels of H4K16ac within 90
174 minutes, cells expressing NLS-BFP-actin^{R62D} sustained mitotic levels of these histone
175 modifications (Supplementary Fig. 4c). In addition, we found higher nuclear levels of Aurora B, a
176 kinase responsible for H3S10 phosphorylation [23], as well as a lower levels of KAT5, known to
177 mediate H4K16 acetylation[24], in cells expressing Flag-NLS-actin^{R62D} (Supplementary Fig. 4d, e).
178 Consistently, chromatin obtained from cells exiting mitosis and expressing NLS-BFP-actin^{R62D}
179 appeared more resistant to MNase digestion (Supplementary Fig. 4f), arguing for reduced
180 chromatin accessibility.

181 Furthermore, electron microscopy of cryopreserved samples allowed us to directly
182 quantify the amount of condensed chromatin, which appears as an electron-dense structure in
183 unlabeled samples (Fig. 4j and Supplementary Fig. 4g). This approach confirmed a highly
184 significant increase in the proportion of condensed chromatin at mitotic exit in cells expressing
185 either nuclear-targeted actin^{R62D} (Fig. 4j, k) or Exportin 6 (Fig. 4l and Supplementary Fig. 4h)
186 compared to control. Altogether, these data support a requirement for polymerization-
187 competent nuclear actin to achieve proper chromatin organization after mitosis.

188

Nuclear F-actin is formed and required for nuclear volume expansion in early mouse embryos

To gain insight into the biological consequences of impaired mitotic nuclear actin assembly we determined general transcriptional activity by quantifying nuclear 3D RNA polymerase II phospho-Serine 5 (pS5) fluorescence. This revealed strongly reduced transcriptional activity in cells expressing GFP-Exportin 6 (Fig. 5a and Supplementary Fig. 5a) as well as significantly lower proliferation rates (Fig. 5b).

Next, we asked if similar functions of nuclear F-actin are exerted during development. For this, we investigated fertilized mouse embryos, which rely on substantial chromatin decondensation of sperm and oocyte nuclei. 150 ng mRNA of nAC-GFP was injected into mouse fertilized embryos and analyzed at indicated time points post insemination (hpi) (Fig. 5c). Notably, nuclear actin filaments were readily detected in pronuclei, as well as in the early G_1 phase after the first mitotic division (71.43%, 18 hpi) and disassembled upon further cell cycle progression of the 2-cell embryos (25%, 24 hpi) (Fig. 5d). Of note, expression of actin^{R62D}-HA-NLS or Exportin 6 inhibited nuclear volume expansion after the first mitotic division (Fig. 5e, f), consistent with our findings in mammalian somatic cells. Furthermore, a significant developmental delay was observed in Exportin 6 mRNA-injected embryos (Fig. 5g and Supplementary Fig. 5b), providing further evidence for a physiological role of nuclear F-actin assembly in the early steps of mouse embryo development.

Cofilin-1 controls nuclear F-actin assembly, volume expansion and chromatin organization in daughter cell nuclei

As siRNA against several known actin assembly factors had no obvious effect on nuclear F-actin formation (Supplementary Table 1) and to gain further mechanistic insight, we performed a proteomic screen using biotin-phalloidin to identify potential nuclear F-actin binding proteins from nuclear fractions of cells released from a mitotic nocodazole arrest (Fig. 6a, b). Hereby, we identified the F-actin disassembly factor Cofilin-1 as a candidate interactor (Fig. 6c, d and Supplementary Table 1). Since Cofilin-1 is inactivated by phosphorylation on Ser-3 (p-Cofilin) [25], we analyzed nuclear p-Cofilin levels by measuring 3D nuclear fluorescence intensities in synchronized NIH3T3 cells and observed a pronounced increase in nuclear p-Cofilin levels during mitotic exit, revealing Cofilin-1 as a cell cycle-controlled nuclear actin regulator (Fig. 6e and Supplementary Fig. 6a-d). Indeed, and consistent with the role of Cofilin-1 in F-actin disassembly, siRNA against Cofilin-1 resulted in a pronounced stabilization of nuclear F-actin during mitotic exit (Fig. 6f, g and Supplementary Video 5).

To specifically address the nuclear function of Cofilin-1 during this cell cycle phase, we generated cells expressing either wildtype (WT-Cofilin) or cytoplasm-targeted Cofilin-1 (NES-Cofilin; NES, nuclear export signal) resistant to siRNA targeting (Fig. 6h, i). Imaging mitotic cells revealed that upon silencing of endogenous Cofilin-1, cells devoid of its nuclear localization failed to prevent extensive nuclear F-actin stabilization during mitotic exit (Fig. 6j and Supplementary Fig. 6e) similar to depletion of total Cofilin-1 (Fig. 6g). Consistent with deregulated actin filament dynamics and turnover, this resulted in defective nuclear volume expansion (Fig. 6k) and chromatin decompaction (Fig. 6l), underscoring the critical importance of dynamic F-actin reorganization for the processes of nuclear volume expansion and chromatin reorganization.

Optogenetic control of Cofilin-1 establishes its role in reorganizing daughter cell nuclei after mitosis

To corroborate our findings that nuclear Cofilin-1 controls chromatin dynamics, we expressed a nuclear-targeted version of Cofilin-1 (NLS-Cofilin) to inhibit nuclear F-actin formation in early G_1 (Supplementary Fig. 6f), and observed a striking defect in establishing open chromatin in cryo-EM samples (Fig. 7a, b).

To directly and reversibly control Cofilin-1 function within the nucleus in real time, we generated an optogenetic Cofilin-1 (opto-Cofilin) (Fig. 7c) based on a previously described light-inducible nuclear export system [26]. Under control conditions, opto-Cofilin exhibited a subcellular distribution similar to WT-cofilin, but allowed for rapid and efficient light-induced nuclear export within 200 seconds, which could be reverted within 500 seconds after illumination was switched off (Fig. 7d and Supplementary Video 6).

In cells silenced for endogenous Cofilin-1 (Supplementary Fig. 6g), light-induced nuclear export of opto-Cofilin resulted in extensive stabilization of nuclear F-actin during mitotic exit (Fig. 7e and Supplementary Videos 7, 8), while its timely controlled nuclear re-accumulation, by switching off illumination, triggered rapid re-organization and successive disassembly of nuclear F-actin (Fig. 7e and Supplementary Video 8). Notably, light-controlled export of opto-Cofilin during mitotic exit also resulted in arrested growth of daughter cell nuclei, while nuclear reimport of opto-Cofilin promoted their further volume expansion (Fig. 7f).

Together, these results uncover a critical nuclear-specific function of Cofilin-1 in spatiotemporally controlling actin dynamics for nuclear reorganization in the early phases after mitotic cell division.

DISCUSSION

Here, we discovered dynamic and transient F-actin assembly in the growing nuclei of daughter cells exiting mitosis. The mechanisms and cellular factors that determine nuclear volume regulation are poorly understood [11]. Our data reveal a key function for nuclear actin filaments in nuclear volume and chromatin expansion during mitotic exit as well as a critical nuclear function of Cofilin-1 in tightly controlling the spatiotemporal turnover of these actin filaments. As such, nuclear reorganization during mitotic exit is impaired upon loss of polymerization-competent nuclear actin as well as excessive nuclear F-actin formation, illustrating that the dynamic interplay between polymerization and depolymerization of nuclear F-actin appears to be critical during this cell cycle-specific process. Accordingly, it is tempting to speculate that additional actin-regulatory factors as well as actin bundling proteins are involved in nuclear actin assembly during early G_1.

Since cytoskeletal actin dynamics are well known to exert contractile and mechanical forces in order to shape or move a variety of cellular components [27] and in light of our observation of F-actin-dependent nuclear protrusions, one may envisage similar functions for nuclear F-actin during mitotic exit in rearranging the chromatin and nuclear content of mammalian cells. Thus, future work will be directed to dissect whether the role for nuclear

actin in promoting efficient reorganization of chromatin is primarily exerted through direct effects of F-actin on chromatin, or more indirectly through expanding and reshaping the nuclear compartment, or both.

Our findings thus open a perspective to gain a better understanding of nuclear actin filament dynamics and its role in regulating spatiotemporal chromatin organization and maintenance of a defined nuclear architecture, all of which have profound implications for genome stability and regulation in health and disease.

References:

1. Bezanilla, M., Gladfelter, A. S., Kovar, D. R. & Lee, W.-L. Cytoskeletal dynamics: a view from the membrane. *J. Cell Biol.* **209,** 329–37 (2015).

2. Grosse, R. & Vartiainen, M. K. To be or not to be assembled: progressing into nuclear actin filaments. *Nat. Rev. Mol. Cell Biol.* **14,** 693–7 (2013).

3. Belin, B. J. & Mullins, R. D. What we talk about when we talk about nuclear actin. *Nucleus* **4,** 291–7 (2013).

4. Kapoor, P., Chen, M., Winkler, D. D., Luger, K. & Shen, X. Evidence for monomeric actin function in INO80 chromatin remodeling. *Nat. Struct. Mol. Biol.* **20,** 426–432 (2013).

5. Cao, T. *et al.* Crystal structure of a nuclear actin ternary complex. *Proc. Natl. Acad. Sci. U. S. A.* **113,** 8985–90 (2016).

6. Virtanen, J. A. & Vartiainen, M. K. Diverse functions for different forms of nuclear actin.

Curr. Opin. Cell Biol. **46,** 33–38 (2017).

7. Baarlink, C., Wang, H. & Grosse, R. Nuclear actin network assembly by formins regulates the SRF coactivator MAL. *Science* **340,** 864–7 (2013).

8. Plessner, M., Melak, M., Chinchilla, P., Baarlink, C. & Grosse, R. Nuclear F-actin formation and reorganization upon cell spreading. *J. Biol. Chem.* **290,** 11209–11216 (2015).

9. Belin, B. J., Lee, T. & Mullins, R. D. DNA damage induces nuclear actin filament assembly by Formin -2 and Spire-½ that promotes efficient DNA repair. [corrected]. *Elife* **4,** e07735 (2015).

10. Plessner, M. & Grosse, R. Extracellular signaling cues for nuclear actin polymerization. *Eur. J. Cell Biol.* **94,** 359–62 (2015).

11. Webster, M. *et al.* Sizing up the nucleus: nuclear shape, size and nuclear-envelope assembly. *J. Cell Sci.* **122,** 1477–86 (2009).

12. Gerlich, D., Beaudouin, J., Gebhard, M., Ellenberg, J. & Eils, R. Four-dimensional imaging and quantitative reconstruction to analyse complex spatiotemporal processes in live cells. *Nat. Cell Biol.* **3,** 852–855 (2001).

13. Schooley, A., Vollmer, B. & Antonin, W. Building a nuclear envelope at the end of mitosis: Coordinating membrane reorganization, nuclear pore complex assembly, and chromatin de-condensation. *Chromosoma* **121,** 539–554 (2012).

14. Burke, B. & Ellenberg, J. Remodelling the walls of the nucleus. *Nat. Rev. Mol. Cell Biol.* **3,** 487–497 (2002).

15. Strzelecka, M. & Heald, R. RUVs Drive Chromosome Decondensation after Mitosis. *Dev. Cell* **31,** 259–260 (2014).

16. Magalska, A. *et al.* RuvB-like ATPases Function in Chromatin Decondensation at the End of Mitosis. *Dev. Cell* **31,** 305–318 (2014).

17. Lombardi, M. L. *et al.* The interaction between nesprins and sun proteins at the nuclear envelope is critical for force transmission between the nucleus and cytoskeleton. *J. Biol. Chem.* **286,** 26743–53 (2011).

18. Posern, G., Sotiropoulos, A. & Treisman, R. Mutant actins demonstrate a role for unpolymerized actin in control of transcription by serum response factor. *Mol. Biol. Cell* **13,** 4167–4178 (2002).

19. Chen, Q., Nag, S. & Pollard, T. D. Formins filter modified actin subunits during processive elongation. *J. Struct. Biol.* **177,** 32–9 (2012).

20. Kaidi, A. & Jackson, S. P. KAT5 tyrosine phosphorylation couples chromatin sensing to ATM signalling. *Nature* **498,** 70–4 (2013).

21. Llères, D., James, J., Swift, S., Norman, D. G. & Lamond, A. I. Quantitative analysis of chromatin compaction in living cells using FLIM–FRET. *J. Cell Biol.* **187,** 481–496 (2009).

22. Wilkins, B. J. *et al.* A cascade of histone modifications induces chromatin condensation in mitosis. *Science* **343,** 77–80 (2014).

23. Wei, Y., Yu, L., Bowen, J., Gorovsky, M. a & Allis, C. D. D. Phosphorylation of histone H3 is required for proper chromosome condensation and segregation. *Cell* **97,** 99–109 (1999).

24. Kimura, A. & Horikoshi, M. Tip60 acetylates six lysines of a specific class in core histones in vitro. *Genes Cells* **3,** 789–800 (1998).

25. Mizuno, K. Signaling mechanisms and functional roles of cofilin phosphorylation and dephosphorylation. *Cell. Signal.* **25,** 457–469 (2013).

26. Niopek, D., Wehler, P., Roensch, J., Eils, R. & Di Ventura, B. Optogenetic control of nuclear protein export. *Nat. Commun.* **7,** 10624 (2016).

27. Blanchoin, L., Boujemaa-Paterski, R., Sykes, C. & Plastino, J. Actin dynamics, architecture, and mechanics in cell motility. *Physiol. Rev.* **94,** 235–63 (2014).

Supplementary Information is linked to the online version of the paper at www.nature.com/nature.

Acknowledgments: We thank members of our laboratory for discussions, P. Chinchilla, G. Pathria, M. Losekam, A. Takasu, H. Hatano, K. Matsumoto, and K. Yamagata for technical assistance, A. Herman and L. S. Ballesteros for cell sorting and B. Di Ventura for critical reading of the manuscript. This work was funded by a HFSP collaborator program grant RGP0021/2016-GROSSE to K.M., A.K. and R.G. Work in the R.G. laboratory is supported by the Deutsche Forschungsgemeinschaft (DFG) (GR 2111/7-1), and the Wilhelm-Sander-Stiftung 2013.149.1. A.K. is funded by a MRC New Investigator Award (MR/N000013/1) and a Wellcome Trust Seed Awards in Science (WT107789AIA). K.M. is funded by JSPS KAKENHI Grant (JP16H01321, JP16H01222). AFM was carried out in the Chemical Imaging Facility, University of Bristol funded

353 by EPSRC (EP/K035746/1), and FLIM was carried out at the Wolfson Bioimaging Facility,
354 University of Bristol, a BBSRC/EPSRC-funded Synthetic Biology Research Centre (L01386X).

355

356 **Author Contributions:** C.B., M.P. and R.G. conceived the study. C.B., M.P., and A.S. performed
357 and analysed most of the experiments with help from R.G. and A.K.; R.H. assisted in electron
358 microscopy, D.A. in FLIM/FRET; K.Mo., S.M. and K.Mi. performed experiments on fertilized
359 mouse embryos; E.M.K, D.V. and U.E. performed PALM/STORM, and S.B. mass spectrometry.
360 R.G. and C.B. wrote the manuscript.

361 **Author Information:** Reprints and permissions information is available at
362 www.nature.com/reprints. The authors declare no competing financial interests.
363 Correspondence and requests for materials should be addressed to R. G.
364 (robert.grosse@staff.uni-marburg.de).

Figure Legends

Figure 1 | Spatiotemporal features and dynamics of nuclear F-actin formation at mitotic exit. **(a)** Time-lapse imaging of NIH3T3 cells stably expressing nAC-GFP (nuclear Actin-Chromobody-GFP, anti-Actin-Chromobody-GFP-NLS, green, grey in magnifications) together with LifeAct-mCherry (red) during anaphase and mitotic exit. The asterisk indicates a nucleus shown magnified in the lower panel. Images show maximum intensity projections of confocal z-stacks. See also Supplementary Video 1. Scale bar, 10 µm; time stamp, h:min:s. **(b)** Live cell imaging of NIH3T3 cells stably expressing nAC-GFP (green) together with Lamin-Cb-SNAP (Lamin-Chromobody-SNAP, labelled by SiR-647, magenta) during mitotic exit. The nucleus indicated by an asterisk is shown magnified for individual time points. See also Supplementary Video 2. Scale bar, 10 µm (overview) and 1 µm (magnifications). **(c)** Quantification of incidence and **(d)** duration of nuclear actin filament formation at mitotic exit using indicated nuclear actin probes. Data are shown as mean + SEM from at least n=3 independent experiments and n=60 (nAC-GFP), n=30 (sAC-GFP, shuttling Actin-Chromobody, anti-Actin-Chromobody-GFP-NLS-NES), n=60 (phalloidin, formaldehyde fixation 70 min after mitotic shake-off) mitotic events. **(e)** NIH3T3 cells at mitotic exit were fixed using glutaraldehyde and stained for actin filaments using phalloidin-Atto 488. The area indicated by a dashed rectangle is shown magnified for individual confocal slices in z-direction with a step size of 0.37 µm. Scale bar, 10 µm (overview) and 1 µm (magnifications).

Figure 2 | Super-resolution microscopy reveals structural features of nuclear F-actin at mitotic exit.

(a) Photoactivated localization microscopy (PALM) of nuclear actin filaments in fixed NIH3T3 cells stably expressing nAC-Dendra2 (anti-Actin-Chromobody-Dendra2-NLS, orange) at mitotic exit. DIC (differential interference contrast) images were acquired over time to monitor mitotic progression and to allow for time-defined fixation 20 min after anaphase. Experimental resolution after drift correction is 33 ± 1 nm. Scale bars, 5 µm. **(b)** Filament widths of nAC-Dendra2-labeled nuclear actin filaments (n = 81, data were collected from at least n=3 independent experiments) as histograms (up) with a bin size of 10.65 nm (x-axis) plotted against frequency (y-axis). Full data is represented underneath the histograms as box + scatter plots with the same x-axis. The box marks the first and third quartiles and the indent represents the median. Whiskers mark minimal and maximal values. **(c)** Stochastic Optical Reconstruction Microscopy (STORM) of phalloidin-stained nuclear actin filaments in native NIH3T3 cells at mitotic exit. The overview image focuses on a nucleus 45 min after anaphase (see also Supplementary Fig. 2c). The magnifications show representative thin (1) and thick (2) filaments with different labelling densities. Scale bars, 5 µm (overview) and 200 nm (magnifications). **(d)** Filament widths of phalloidin-labelled nuclear actin filaments (n=53, data were collected from n=1 experiment) as histograms (up) with a bin size of 14.3 nm (x-axis) plotted against frequency (y-axis). Full data is represented underneath the histograms as box + scatter plots with the same x-axis. The box marks the first and third quartiles and the indent represents the median. Whiskers mark minimal and maximal values.

Figure 3 | Nuclear F-actin reshapes nuclei, and promotes nuclear volume expansion after mitotic cell division.

409 **(a)** NIH3T3 cells stably expressing nAC-GFP (green) together with H2B-mCherry (red) during
410 mitotic exit. Asterisk indicates the nucleus shown for additional time points. Dashed rectangles
411 indicate areas of dynamic nuclear protrusions, shown magnified over time. Arrows indicate
412 direction of protrusions. See also Supplementary Video 4. Scale bar, 10 µm (overviews) and 1
413 µm (magnifications); time stamp, min:s. **(b)** NIH3T3 cells expressing nAC-GFP (green) together
414 with mCherry or mCherry-Exportin 6 (gray, insets) after anaphase. Figures give proportion of
415 cells showing nuclear F-actin in the presence (n=15) or absence (n=17 mitotic events) of GFP-
416 Exportin 6, visualized by nAC-mCherry. Scale bar, 10 µm. **(c)** Nuclear expansion after anaphase
417 (00:00) was visualized by H2B-mCherry in NIH3T3 cells expressing GFP or GFP-Exportin 6.
418 Images show representative coloured 3D surface reconstructions of daughter nuclei. Time
419 stamp, h:min. **(d)** Quantification of nuclear volume during mitotic exit in NIH3T3 cells
420 expressing either GFP or GFP-Exportin 6. Data shows mean ± SEM from n=4 independent
421 experiments and n=30 nuclei per condition. **(e)** Images of NIH3T3 cells stably expressing nAC-
422 GFP (green) together with doxycycline-induced BFP-NLS or NLS-BFP-actin^{R62D} (gray, insets) at
423 mitotic exit. Figures give proportion of cells showing nuclear F-actin (BFP-NLS, n=22; NLS-BFP-
424 actin^{R62D}, n=18 mitotic events). Scale bar, 10 µm. **(f)** Visualization of nuclear expansion in
425 NIH3T3 cells expressing doxycycline-induced BFP-NLS or NLS-BFP-actin^{R62D} similar to **c**. **(g)**
426 Quantification of nuclear volume during mitotic exit in NIH3T3 cells expressing doxycycline-
427 induced BFP-NLS or actin derivatives, as indicated. Data shows mean ± SEM from n=3
428 independent experiments and n=60 (BFP-NLS, NLS-BFP-actin^{R62D}), n=50 nuclei (Flag-NLS-actin^{wt},
429 Flag-NLS-actin^{R62D}). **(h)** Representative AFM images show nuclear surface morphology of
430 isolated NIH3T3 nuclei. Early G_1 nuclei were obtained from cells expressing Flag-NLS-actin^{wt} or

Flag-NLS-actin^{R62D}, whereas interphase nuclei were treated with or without TSA (1 µM, 5 h) to induce chromatin decondensation. Scale bar, 1 µm. **(i)** Quantification of surface roughness of early G_1 nuclei expressing Flag-NLS-actin^{wt} or Flag-NLS-actin^{R62D}. Data shows mean ± SEM from n=2 independent experiments and n=9 nuclei per condition; P values were calculated by *t*-test. **(j)** Quantification of surface roughness of control or TSA-treated interphase nuclei. Data shows mean ± SEM from n=2 independent experiments and n=7 nuclei per condition. P values were calculated by *t*-test.

Figure 4 | Nuclear actin dynamics promote chromatin decondensation at mitotic exit.

(a) NIH3T3 cells stably expressing a shuttling Actin Chromobody (sAC-GFP, green) together with H2B-mCherry. Asterisk indicates the nucleus shown magnified for additional time points to visualize nuclear F-actin within interchromatin spaces. See also Supplementary Video 3. Scale bars, 10 µm; time stamp, min:s. **(b)** Maximum intensity projections of confocal z-stacks illustrate H2B-mCherry fluorescence densities (grey) during mitotic exit in NIH3T3 cells co-expressing BFP-NLS or NLS-BFP-actin^{R62D}. Scale bar, 10 µm; time stamp, h:min. **(c-e)** Chromatin densities of NIH3T3 cells were assessed in G_0 or 90 min after anaphase (mitotic exit) and compared between **(c)** expression of BFP-NLS and NLS-BFP-actin^{R62D} (each n=60 nuclei), **(d)** expression of Flag-NLS actin^{wt} and Flag-NLS-actin^{R62D} (each n=50 nuclei) or **(e)** expression of GFP and GFP-Exportin 6 (each n=30 nuclei). In each panel data is shown as mean + SEM from n=3 independent experiments. P values were calculated by two-way ANOVA. **(f-i)** Fluorescence lifetime imaging microscopy (FLIM) of fluorescence resonance energy transfer (FRET) between GFP- and H2B-mCherry NIH3T3 cells at mitotic exit. **f** and **h** provide image examples for the

tested conditions. The colour code indicates fluorescence lifetime of GFP-H2B. Scale bar, 10 µm. **(g, i)** Quantifications of GFP-H2B fluorescence lifetime (Tau) in early G_1 NIH3T3 cells expressing either Flag-NLS-actin^{wt} or Flag-NLS-actin^{R62D} **(g)** or Flag-Exportin 6 **(i)**. Data is shown as boxplot of n≥20 **(g)** or n≥30 **(i)** cells per condition from n=3 independent experiments. P values were calculated by *t*-test. See also Supplementary Fig. 4a, b. **(j)** Representative electron microscopy images of cryo-preserved, synchronized early G_1 NIH3T3 cells induced to express BFP-NLS or NLS-BFP-actin^{R62D}. Areas indicated by a dashed rectangle are shown magnified. Scale bar, 2 µm. **(k, l)** Quantifications of condensed chromatin based on cryo-EM images. Chromatin condensation was compared between control conditions and expression of either NLS-BFP-actin^{R62D} (n≥28 nuclei) **(k)** or expression of GFP-Exportin 6 (n≥14 nuclei) **(l)**. In each panel data is shown as mean + SEM from n=2 independent experiments. P values were calculated by *t*-test.

Figure 5 | Inhibition of nuclear F-actin formation impairs transcription, proliferation and early embryonic development.

(a) 3D quantification of nuclear RNA Pol II pS5 fluorescence intensities in NIH3T3 cells expressing either GFP or GFP-Exportin 6 at indicated time points after mitotic shake off. See also Supplementary Fig. 5a. Data are shown as mean + SD from n=2 independent experiments and n≥10 nuclei per condition. P values were calculated by two-way ANOVA. **(b)** Proliferation of NIH3T3 cells expressing either GFP or GFP-Exportin 6 was measured using WST-1. Data were normalized to values of control cells at time 0 h and are shown as mean + SEM from n=3 independent experiments. P values were calculated by two-way ANOVA. **(c)** Experimental scheme for studying nuclear F-actin in fertilized mouse embryos. At 2 hpi (hours post

insemination) mRNA encoding for the indicated proteins was injected into fertilized embryos to either visualize or manipulate nuclear actin dynamics. **(d)** Image examples showing early embryo development at 8 hpi (pronuclei), 18 hpi and 24 hpi (2-cell). DIC, Differential interference contrast. Nuclear F-actin corresponding to dashed rectangles is shown magnified below (nAC-GFP, green). Scale bars, 20 µm (overview) and 10 µm (magnifications). **(e, f)** Image examples and quantitative analysis of nuclear volume in 2-cell embryos expressing either actin^{R62D}-HA-NLS or actin^{wt}-HA-NLS **(e)** or mCherry-Exportin 6 **(f)**. Scale bar, 20 µm. Quantitative data is shown as mean + SD from n=3 independent experiments and n≥30 nuclei per condition. P values were calculated by *t*-test. **(g)** Preimplantation development of embryos after a single injection of mCherry-Exportin 6 mRNA. Note the significant developmental delay at 48 hpi, 60 hpi, 72 hpi and 96 hpi compared to injection of mRNA encoding myc-tagged GFP. Data is shown as mean + SEM from n=3 independent experiments. P values were calculated by chi-squared test. See also Supplementary Fig. 5b.

Figure 6 | Nuclear Cofilin-1 regulates nuclear F-actin during mitotic exit.

(a) Cartoon illustrating nuclear F-actin pulldown at mitotic exit. **(b)** Immunoblot detecting α-Tubulin (cytoplasm) and Histone 3 (H3, nucleus) confirms successful subcellular fractionation. **(c)** Immunoblot detecting β-actin and Cofilin-1 validates efficient pulldown of nuclear F-actin and co-precipitation of Cofilin-1. **(d)** Table listing nuclear F-actin-binding proteins as identified by mass spectrometry (cov., coverage). **(e)** 3D quantitative immunofluorescence analysis of nuclear p-Cofilin at indicated times after mitotic shake-off. Data are shown as mean + SD from n=30 mitotic events for each time point. See also Supplementary Fig. 6a, b. **(f)** Time-lapse

497 imaging shows nAC-GFP expressing NIH3T3 cells transfected with si-control or si-Cofilin at
498 indicated times after anaphase. See also Supplementary Video 5. Scale bar, 5 µm; time stamp,
499 h:min. **(g)** Quantifications of stabilized nuclear F-actin (present for ≥2 h after anaphase) in
500 NIH3T3 cells treated with indicated siRNAs. Data are shown as mean + SD from n=3
501 independent experiments and n=49 (si-control), n=58 (si-Cofilin), n=59 (si-Cofilin (3'-UTR))
502 mitotic events. Immunoblot confirms efficient silencing of Cofilin-1. **(h)** Confocal images of fixed
503 NIH3T3 cells stably expressing WT- or NES-mCherry-Cofilin (red). Scale bar, 10 µm. **(i)**
504 Immunoblot of NIH3T3 cells stably expressing WT- or NES-mCherry-Cofilin confirms siRNA (si-
505 Cofilin (3' UTR))-resistant expression of mCherry-Cofilin derivatives. **(j)** Quantifications of
506 stabilized nuclear F-actin (present for ≥2.5 h after anaphase) in NIH3T3 cells treated with si-
507 Cofilin (3'-UTR) in the presence of either WT- or NES-mCherry-Cofilin. Data are shown as mean
508 + SD from n=3 independent experiments and n=30 (WT), n=38 (NES) mitotic events. **(k)**
509 Quantifications of nuclear volume during mitotic exit in NIH3T3 cells treated with si-control or
510 si-Cofilin (3'-UTR) in the presence of either WT- or NES-mCherry-Cofilin. Data are shown as
511 mean + SD from n=3 independent experiments and n=50 nuclei per condition. **(l)** NIH3T3 cells
512 expressing WT- or NES-mCherry-Cofilin were treated with si-control or si-Cofilin (3'-UTR) and
513 chromatin densities were assessed 90 min after anaphase. Data are shown as mean + SEM from
514 n=3 independent experiments and n=50 nuclei per condition. Unprocessed original scans of
515 blots are shown in Supplementary Fig. 7.
516
517 **Figure 7 | Nuclear Cofilin-1 affects chromatin organization and its optogenetic control reveals**
518 **critical functions in nuclear F-actin disassembly at mitotic exit.**

519 **(a)** Representative electron microscopy images of cryo-preserved NIH3T3 cells at mitotic exit in
520 the absence or presence of NLS-mCherry-Cofilin. Scale bar, 2 µm. **(b)** Quantifications of
521 condensed chromatin based on cyro-EM images. Data are shown as mean + SEM from n=2
522 independent experiments and n≥15 nuclei per condition. P values were calculated by *t*-test. **(c)**
523 Cartoon illustrating design and photo-convertibility of opto-Cofilin. Blue light induces exposure
524 of a photocaged NES (nuclear export sequence), thereby promoting its nuclear export. **(d)** Time-
525 lapse imaging of NIH3T3 cells demonstrates light-regulated control of opto-Cofilin subcellular
526 localization. NIH3T3 cells stably expressing opto-Cofilin (grey) were imaged at 10 second
527 intervals either with (+ light) or without (- light) additional irradiation by blue laser light (488
528 nm). See also Supplementary Video 6. Scale bar, 10 µm. **(e)** NIH3T3 cells stably expressing nAC-
529 SNAP (labelled by SiR-647, grey) and opto-Cofilin (red) were treated with si-Cofilin (3'-UTR) and
530 imaged during and after mitosis. To promote nuclear export of opto-Cofilin, cells were exposed
531 to blue laser light (488 nm) at 2.5 min intervals (+ light). Note the excessive formation of
532 stabilized nuclear F-actin in the absence of nuclear Cofilin as well as the onset of filament
533 disassembly upon controlled nuclear re-import of opto-Cofilin (- light). See also Supplementary
534 Video 8. Scale bar, 10 µm. **(f)** Nuclear fluorescence intensities of opto-Cofilin (red line) and
535 relative nuclear area (black line) were quantified before and during light-regulated re-import of
536 opto-Cofilin. Nuclear re-import of opto-Cofilin is accompanied by nuclear shape changes and
537 overall nuclear expansion. Data are shown as mean from n=5 nuclei.

538

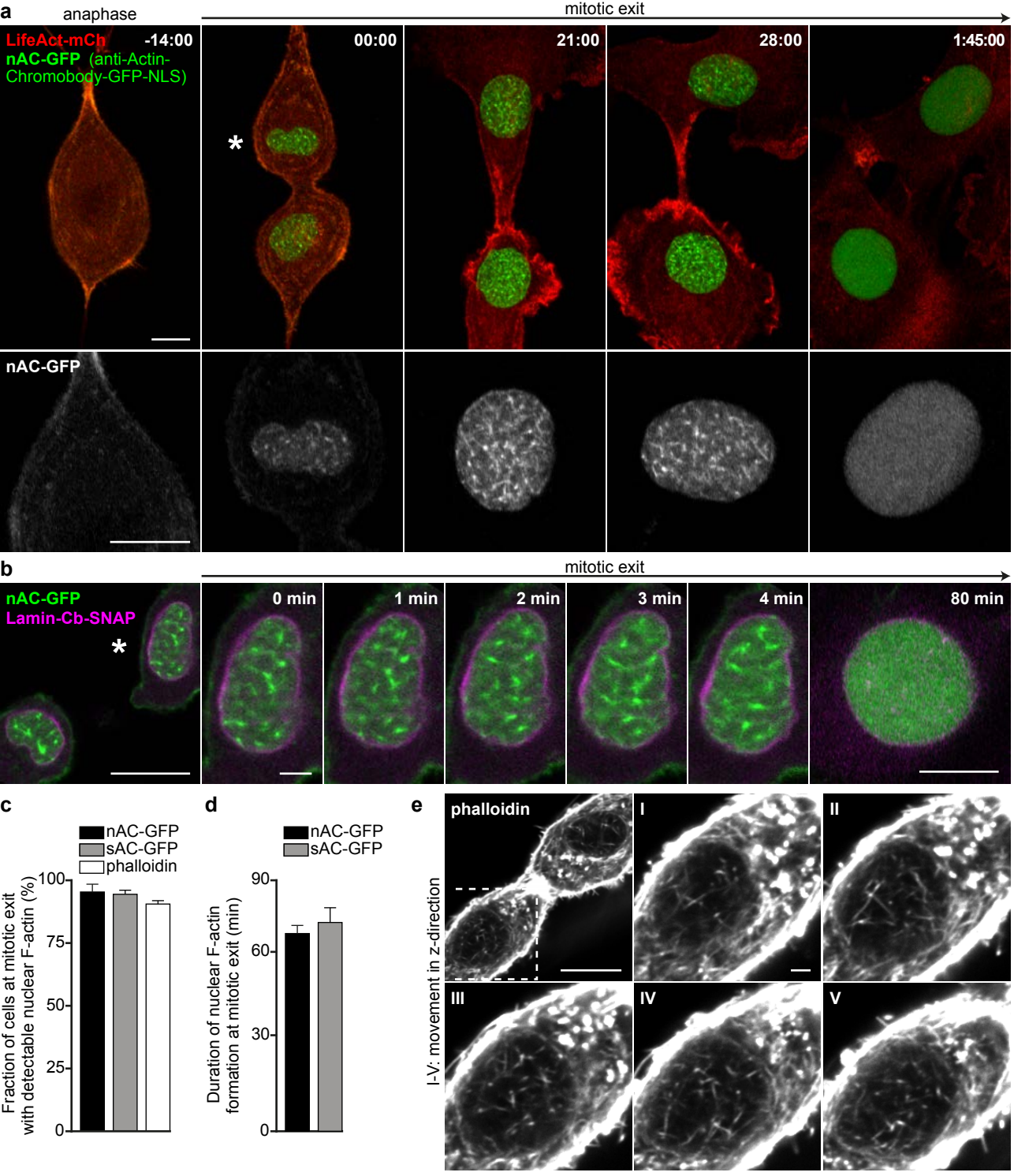
a
anaphase
mitotic exit
LifeAct-mCh
nAC-GFP (anti-Actin-Chromobody-GFP-NLS)
-14:00
00:00
21:00
28:00
1:45:00
nAC-GFP
b
mitotic exit
nAC-GFP
Lamin-Cb-SNAP
0 min
1 min
2 min
3 min
4 min
80 min
c
nAC-GFP
sAC-GFP
phalloidin
Fraction of cells at mitotic exit with detectable nuclear F-actin (%)
100
75
50
25
0
d
nAC-GFP
sAC-GFP
Duration of nuclear F-actin formation at mitotic exit (min)
90
60
30
0
e
phalloidin
I
II
III
IV
V
I-V: movement in z-direction

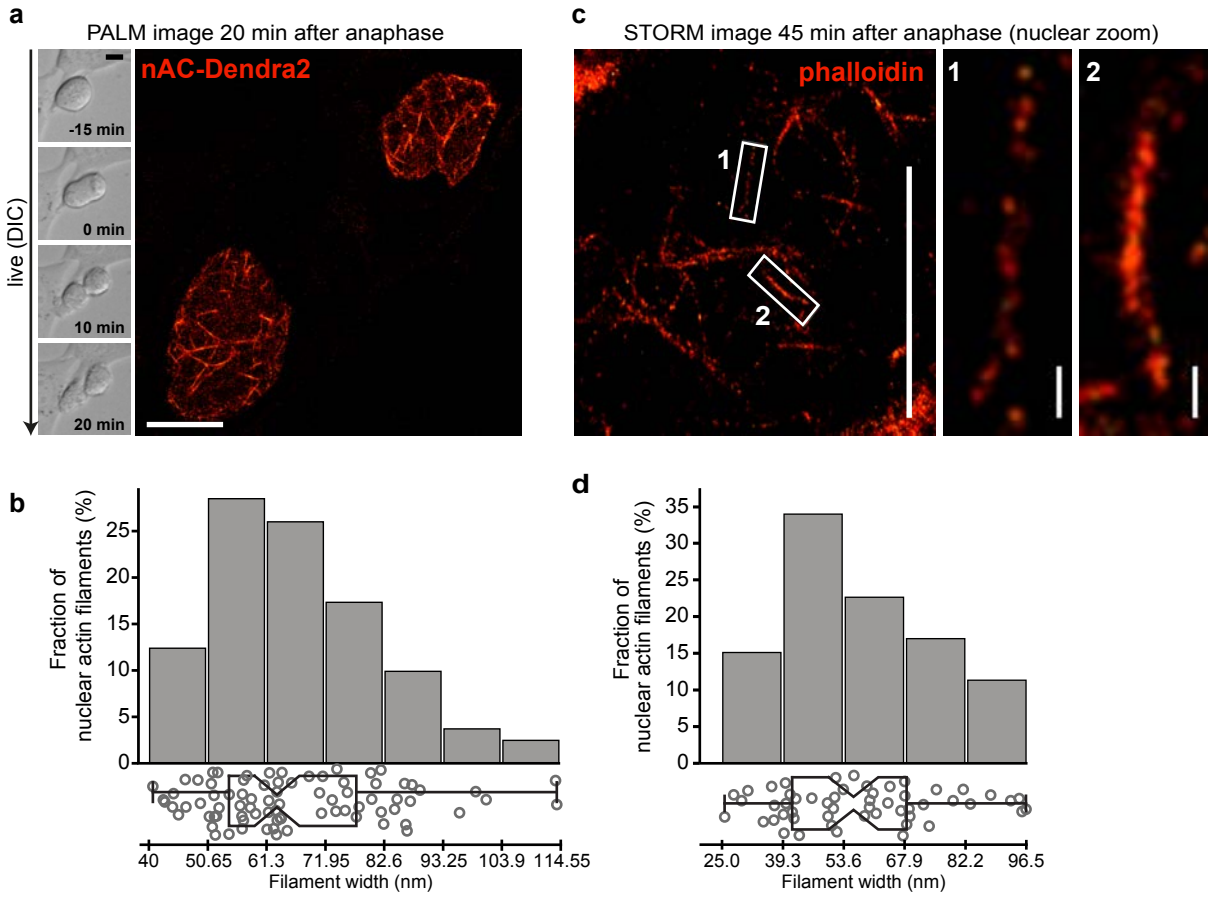
a
PALM image 20 min after anaphase
live (DIC)
-15 min
0 min
10 min
20 min
nAC-Dendra2
c
STORM image 45 min after anaphase (nuclear zoom)
phalloidin
1
2
1
2
b
Fraction of nuclear actin filaments (%)
0
5
10
15
20
25
40
50.65
61.3
71.95
82.6
93.25
103.9
114.55
Filament width (nm)
d
Fraction of nuclear actin filaments (%)
0
5
10
15
20
25
30
35
25.0
39.3
53.6
67.9
82.2
96.5
Filament width (nm)

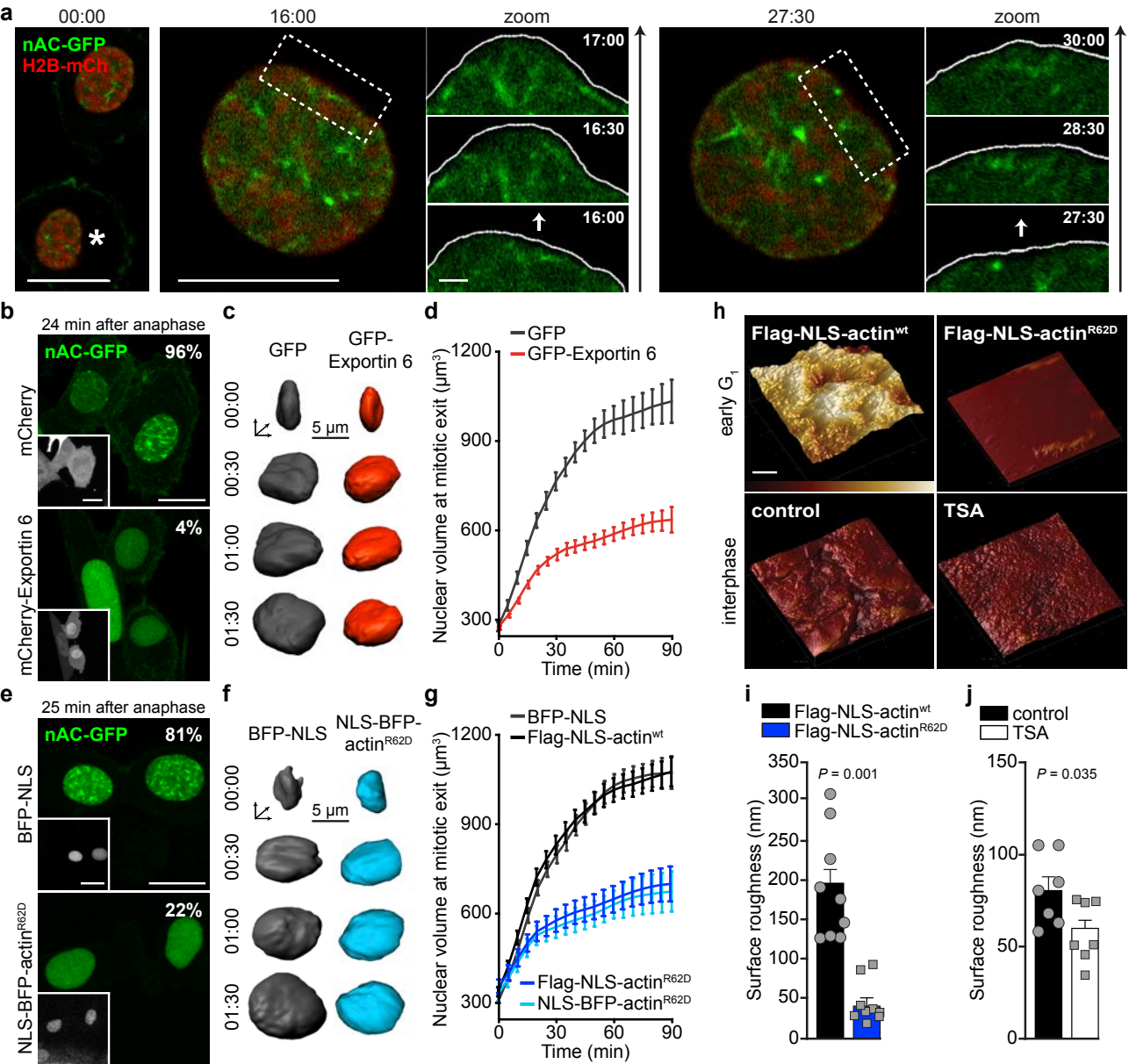
a
00:00
16:00
zoom
27:30
zoom
nAC-GFP
H2B-mCh
17:00
16:30
16:00
30:00
28:30
27:30
b
24 min after anaphase
nAC-GFP
96%
mCherry
4%
mCherry-Exportin 6
c
GFP
GFP-Exportin 6
5 µm
00:00
00:30
01:00
01:30
d
GFP
GFP-Exportin 6
Nuclear volume at mitotic exit (µm³)
1200
900
600
300
0
30
60
90
Time (min)
h
Flag-NLS-actin^wt
Flag-NLS-actin^R62D
early G1
control
TSA
interphase
e
25 min after anaphase
nAC-GFP
81%
BFP-NLS
22%
NLS-BFP-actin^R62D
f
BFP-NLS
NLS-BFP-actin^R62D
5 µm
00:00
00:30
01:00
01:30
g
BFP-NLS
Flag-NLS-actin^wt
Flag-NLS-actin^R62D
NLS-BFP-actin^R62D
Nuclear volume at mitotic exit (µm³)
1200
900
600
300
0
30
60
90
Time (min)
i
Flag-NLS-actin^wt
Flag-NLS-actin^R62D
P = 0.001
Surface roughness (nm)
350
300
250
200
150
100
50
0
j
control
TSA
P = 0.035
Surface roughness (nm)
150
100
50
0

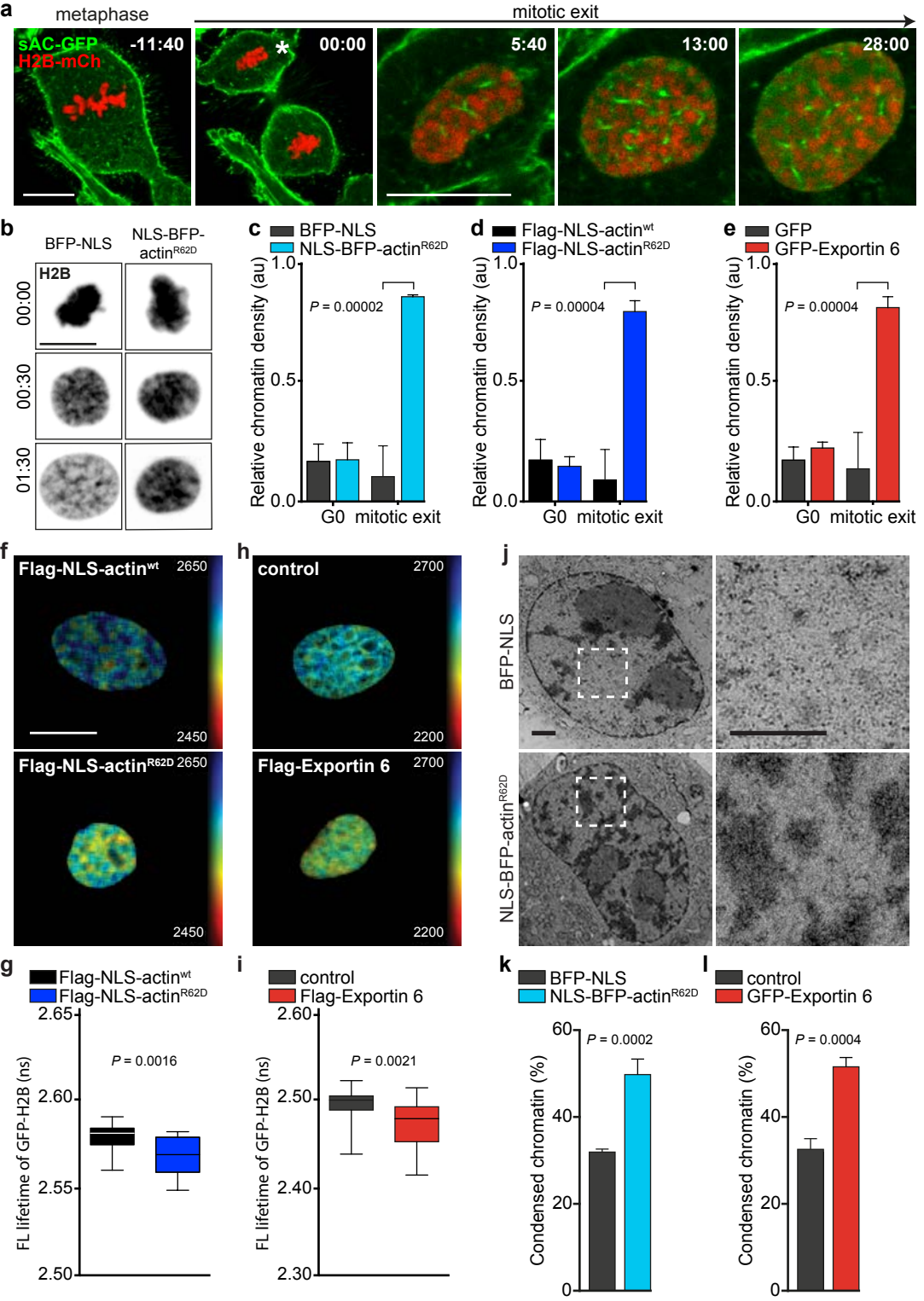
a
metaphase
mitotic exit
sAC-GFP
H2B-mCh
-11:40
00:00
5:40
13:00
28:00
b
BFP-NLS
NLS-BFP-actinR62D
H2B
00:00
00:30
01:30
c
BFP-NLS
NLS-BFP-actinR62D
Relative chromatin density (au)
P = 0.00002
G0
mitotic exit
d
Flag-NLS-actinwt
Flag-NLS-actinR62D
P = 0.00004
e
GFP
GFP-Exportin 6
P = 0.00004
f
Flag-NLS-actinwt
Flag-NLS-actinR62D
h
control
Flag-Exportin 6
j
BFP-NLS
NLS-BFP-actinR62D
g
FL lifetime of GFP-H2B (ns)
P = 0.0016
i
P = 0.0021
k
Condensed chromatin (%)
P = 0.0002
l
P = 0.0004

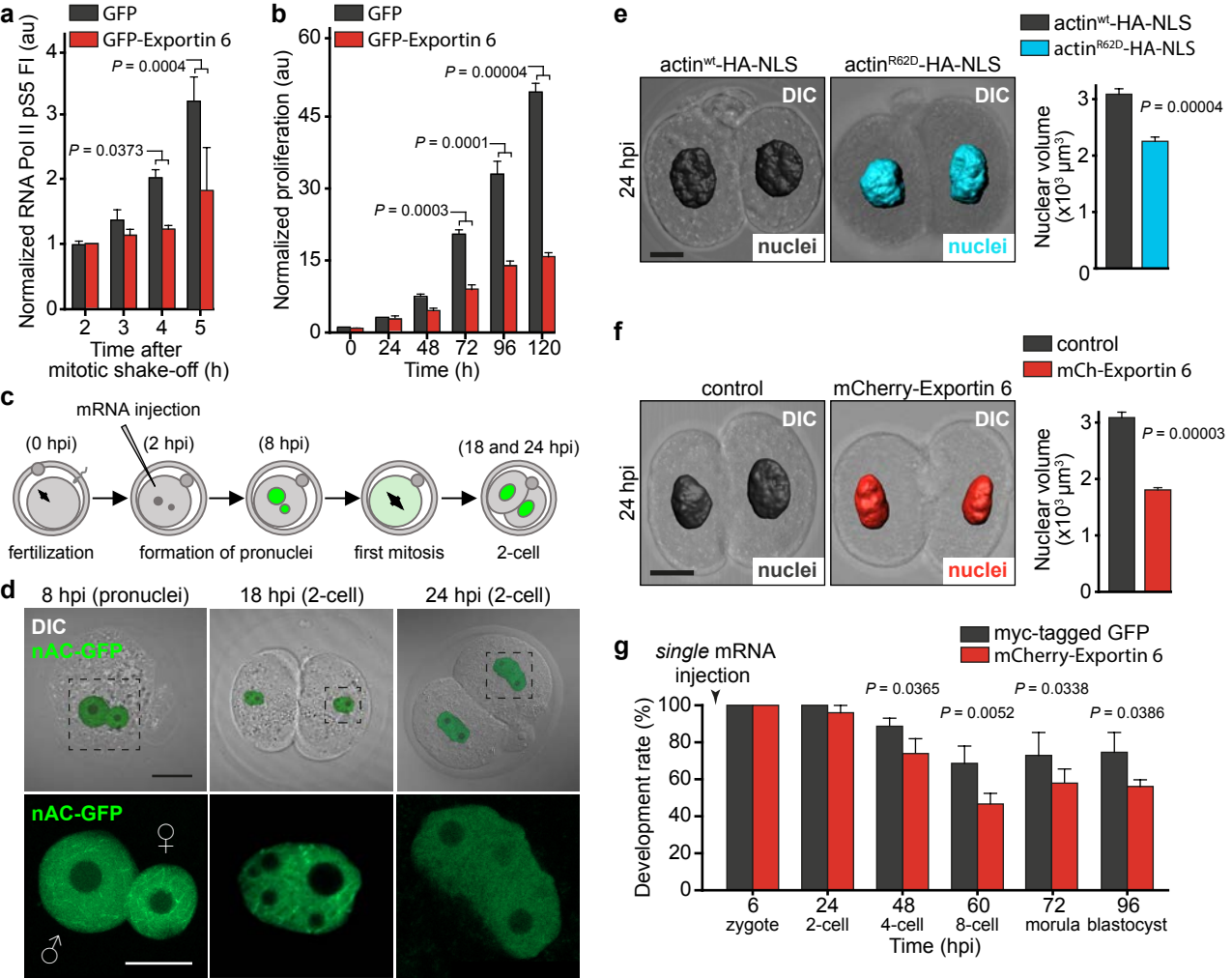
a
GFP
GFP-Exportin 6
Normalized RNA Pol II pS5 FI (au)
P = 0.0004
P = 0.0373
Time after mitotic shake-off (h)
b
GFP
GFP-Exportin 6
Normalized proliferation (au)
P = 0.00004
P = 0.0001
P = 0.0003
Time (h)
c
mRNA injection
(0 hpi)
(2 hpi)
(8 hpi)
(18 and 24 hpi)
fertilization
formation of pronuclei
first mitosis
2-cell
d
8 hpi (pronuclei)
18 hpi (2-cell)
24 hpi (2-cell)
DIC
nAC-GFP
nAC-GFP
e
actinwt-HA-NLS
actinR62D-HA-NLS
actinwt-HA-NLS
actinR62D-HA-NLS
24 hpi
DIC
nuclei
Nuclear volume (x10³ µm³)
P = 0.00004
f
control
mCherry-Exportin 6
control
mCherry-Exportin 6
24 hpi
DIC
nuclei
Nuclear volume (x10³ µm³)
P = 0.00003
g
single mRNA injection
myc-tagged GFP
mCherry-Exportin 6
Development rate (%)
P = 0.0365
P = 0.0338
P = 0.0052
P = 0.0386
6 zygote
24 2-cell
48 4-cell
60 8-cell
72 morula
96 blastocyst
Time (hpi)

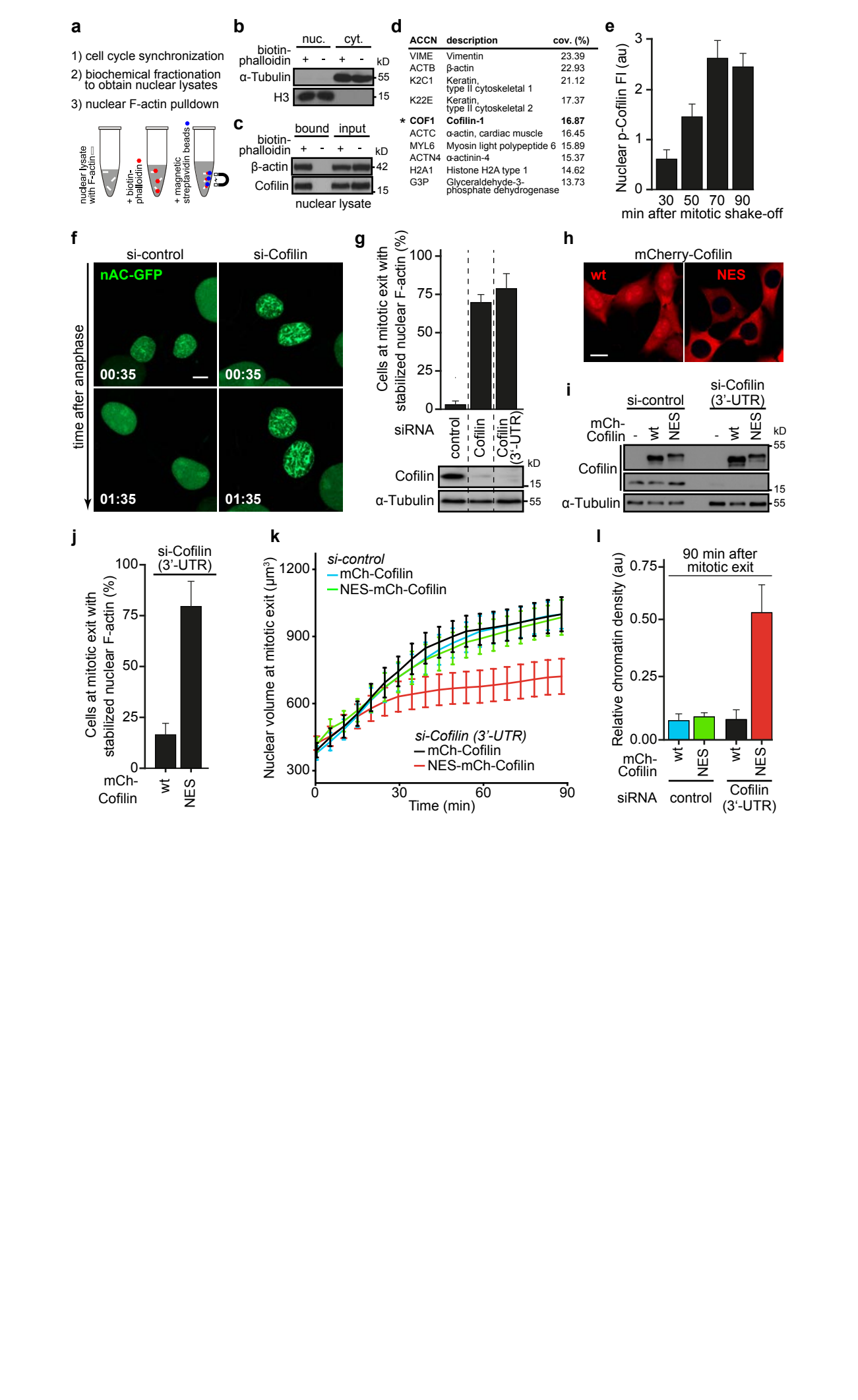
a
1) cell cycle synchronization
2) biochemical fractionation to obtain nuclear lysates
3) nuclear F-actin pulldown
nuclear lysate with F-actin
+ biotin-phalloidin
+ magnetic streptavidin beads
b
nuc.
cyt.
biotin-phalloidin
kD
α-Tubulin
55
H3
15
c
bound
input
biotin-phalloidin
kD
β-actin
42
Cofilin
15
nuclear lysate
d
ACCN description cov. (%)
VIME Vimentin 23.39
ACTB β-actin 22.93
K2C1 Keratin, type II cytoskeletal 1 21.12
K22E Keratin, type II cytoskeletal 2 17.37
* COF1 Cofilin-1 16.87
ACTC α-actin, cardiac muscle 16.45
MYL6 Myosin light polypeptide 6 15.89
ACTN4 α-actinin-4 15.37
H2A1 Histone H2A type 1 14.62
G3P Glyceraldehyde-3-phosphate dehydrogenase 13.73
e
Nuclear p-Cofilin FI (au)
min after mitotic shake-off
f
si-control
si-Cofilin
nAC-GFP
time after anaphase
00:35
01:35
g
Cells at mitotic exit with stabilized nuclear F-actin (%)
siRNA
control
Cofilin
Cofilin (3'-UTR)
kD
Cofilin
α-Tubulin
h
mCherry-Cofilin
wt
NES
i
si-control
si-Cofilin (3'-UTR)
mCh-Cofilin
wt
NES
kD
Cofilin
α-Tubulin
j
si-Cofilin (3'-UTR)
Cells at mitotic exit with stabilized nuclear F-actin (%)
mCh-Cofilin
wt
NES
k
si-control
mCh-Cofilin
NES-mCh-Cofilin
Nuclear volume at mitotic exit (μm³)
si-Cofilin (3'-UTR)
mCh-Cofilin
NES-mCh-Cofilin
Time (min)
l
90 min after mitotic exit
Relative chromatin density (au)
mCh-Cofilin
wt
NES
siRNA
control
Cofilin (3'-UTR)

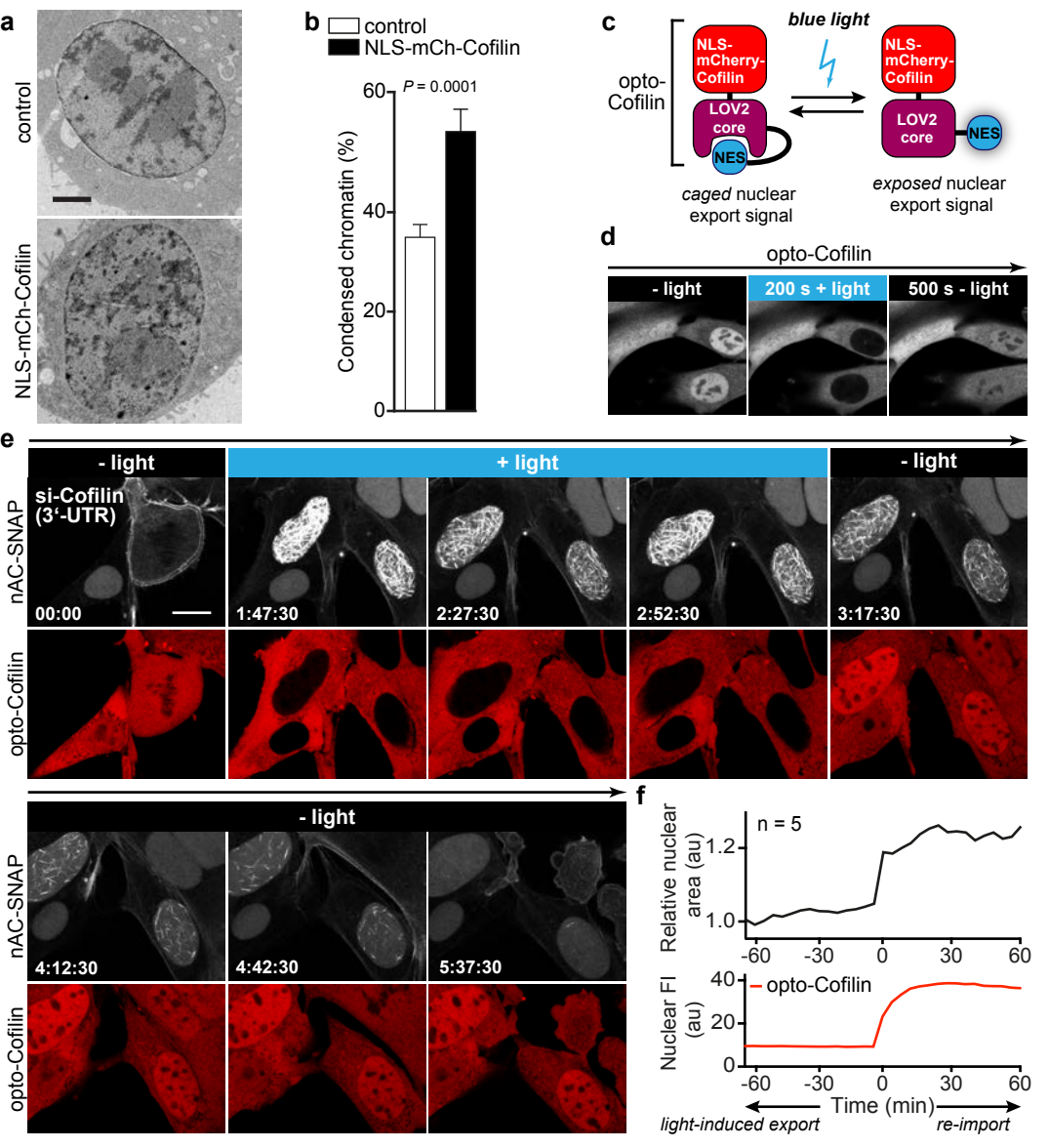
a
control
NLS-mCh-Cofilin
b
control
NLS-mCh-Cofilin
P = 0.0001
Condensed chromatin (%)
60
40
20
0
c
blue light
opto-Cofilin
NLS-mCherry-Cofilin
LOV2 core
NES
caged nuclear export signal
exposed nuclear export signal
d
opto-Cofilin
- light
200 s + light
500 s - light
e
- light
+ light
- light
si-Cofilin (3'-UTR)
nAC-SNAP
opto-Cofilin
00:00
1:47:30
2:27:30
2:52:30
3:17:30
4:12:30
4:42:30
5:37:30
f
n = 5
Relative nuclear area (au)
1.2
1.0
Nuclear FI (au)
opto-Cofilin
40
20
0
-60
-30
0
30
60
Time (min)
light-induced export
re-import

Methods

Antibodies and reagents

Cell culture and transfection reagents (Lipofectamine 2000 and RNAiMax) were obtained from Invitrogen.

Rhodamine-phalloidin, biotin-phalloidin, phalloidin-AF647 and phalloidin-Atto 488 were purchased from Life Technologies. SNAP-Cell 647-SiR was obtained from NEB. SiR-DNA was from Spirochrome. CK-666, Cytochalasin D, DMSO, doxycycline, Latrunculin B, and nocodazole were from Sigma-Aldrich and used at indicated concentrations. Flavopiridol was obtained from Santa Cruz and used at a final concentration of 1 μM.

Information on antibodies used is listed in Table S3.

Plasmids and constructs

The generation of nuclear Actin-Chromobody-GFP (nAC-GFP, anti-actin-Chromobody-GFP-NLS) and sAC was described previously [8]. The nuclear Actin-Chromobody is a genetically encoded, NLS-tagged nanobody against the actin protein. Due to its NLS-fusion, the nuclear Actin-Chromobody is enriched in the nuclei of interphasic cells. Nuclear envelope breakdown in prophase is accompanied by a temporary loss of its specific nuclear localization, which reestablishes during mitotic exit and daughter nuclei assembly.

nAC-Dendra2, nAC-mCherry and nAC-SNAP were generated by replacing the GFP of pWPXL-nAC-GFP by either pDendra2 (Clontech Laboratories, Inc.), mCherry or the SNAP-tag (New England Biolabs).

To obtain a Lamin-nanobody fused to the SNAP-tag, the tagRFP2 of pLC-TagRFP2 (ChromoTek) was replaced by a cDNA encoding the SNAP-tag. For stable expression of

Lamin-nanobody-SNAP, the corresponding cDNA was subcloned into pWPXL using the MluI/SpeI restriction sites.

For stable expression of H2B-mCherry, the GFP of pWPXL was replaced by mCherry, before insertion of a cDNA encoding human H2B via the BamHI/MluI restriction sites.

For generation of tagRFP-KASH, the cDNA of murine Nesprin-1α was amplified as described [17]. KASH was expressed from the EFpLink plasmid carrying a N-terminal tagRFP.

The cDNA of human Exportin 6 was obtained by reverse transcription of total mRNA obtained from HeLa cells. Exportin 6 was expressed from the EFpLink plasmid carrying a N-terminal Flag-, Flag-GFP- or mCherry-tag.

To obtain mCherry-Cofilin plasmids for lentiviral transductions, the cDNA of mouse Cofilin-1 (kindly provided by M. Rust, University of Marburg) was N-terminally fused to mCherry and cloned into pWPXL via MluI/SpeI. For NES-mCherry-Cofilin the NES (nuclear export signal) of HIV1-Rev (LPPLERLTL) was fused to the N-terminus of mCherry. Opto-Cofilin was generated by addition of the cMyc^{P1A} NLS (AAAKRVKLD) to the N-terminus of mCherry-Cofilin and a C-terminal fusion to the LEXY module [26]. Opto-Cofilin was inserted into pWPXL via MluI/SpeI to allow for production of lentiviral particles.

To obtain NLS-BFP-actin^{R62D}, the SV40 large T antigen NLS (PPKKKRKV) was N-terminally fused to tagBFP2 (separated by one linking glycine), which was further fused to the N-terminus of actin^{R62D} [18], separated by a SGLRSRA linker. For BFP-NLS, the cDNA encoding tagBFP2 was C-terminally fused to the SV40 large T antigen NLS, separated by a GDPPVAT linker. To obtain Flag-NLS-actin-T2A-SNAP derivatives, a cDNA encoding human β-actin (either wild-type or containing the point mutation R62D) was N-terminally fused to a Flag-tag and the SV40 large T antigen NLS (separated by a BamH1 restriction site) and C-terminally linked to a SNAP-tag by a self-cleaving T2A peptide (GSGEGRGSLLTCGDVEENPGP).

To allow for stable doxycycline-inducible expression of NLS-BFP-actin^{R62D}, BFP-NLS or Flag-NLS-actin-T2A derivatives, the corresponding cDNAs were inserted into the pInducer20 plasmid [28] by homologous recombination using the Gateway technology (Invitrogen). LifeAct-mCherry lentiviral particles were a gift from O. Fackler (University of Heidelberg).

Cell culture, viral transductions, transfections, and treatments

NIH3T3, HT1080, RPE-1 cells and all their derivatives were grown in DMEM supplemented with 10% FCS (fetal calf serum), 100 U/ml penicillin and 100 mg/ml streptomycin at 37 °C in a 5% CO_2 atmosphere. MCF10A cells and derivatives were cultured as described previously [29].

Lentiviral transductions were performed as previously described [8].

Transient transfections of Exportin 6 or tagRFP-KASH were carried out using Lipofectamine LTX&PLUS Reagent according to the manufacturer's instructions. Transfection of siRNAs and sequence for si-Emerin and si-Lamin A/C have been described previously [8]. In addition, the following siRNAs were obtained from Qiagen: CCGCTGCACCCTGGCAGAGAA (si-Cofilin), TGCCAACTTCTAACCACAATA (si-Cofilin (3'-UTR)), and TTGGACTATCTGACAAGTAAA (si-Exportin 6). Sequences of siRNAs used to obtain data presented in Table S1 are shown within the table.

SNAP-Cell 647-SiR and SiR-DNA were used according to the manufacturer's instructions.

Induction of BFP-NLS, NLS-BFP-actin^{R62D} or Flag-NLS-actin-T2A-SNAP derivatives was achieved by addition of 0.5 µg/ml doxycycline for 16 hours to the cell culture medium. NIH3T3 cells were arrested in G_0 phase by serum starvation (growth medium without FCS) for at least 16 hours.

Immunofluorescence and phalloidin staining

For immunofluorescence stainings, cells were grown on cover slips, before fixation using 4% formaldehyde (15 min at RT). Immunolabeling was performed as described previously [29].

For phalloidin staining in Fig. 1e, cells were fixed using glutaraldehyde according to [7]. Phalloidin staining for the quantification shown in Fig. 1c and for super-resolution microscopy (Fig. 2c,d and Supplementary Fig. 2c) was performed on formaldehyde fixed samples (4% for 15 min at RT). After washing with PBS, samples were incubated with phalloidin-AF647 or phalloidin-Atto 488 at 4°C for 96 hours. For super-resolution microscopy, samples were post-fixed using 1% formaldehyde for 10 min at RT.

Image acquisition and live cell imaging

All confocal image acquisitions were performed on a LSM 700 or LSM 800 confocal laser scanning microscope (Zeiss) equipped with a 63X/1.4 NA oil objective. For live cell imaging, cells were cultured in µ-slides (ibidi) at 37 °C in a 5% CO_2 atmosphere using a humidified incubation chamber (Pecon).

Experiments with opto-Cofilin were carried out using the LSM 800 microscope. To induce nuclear export of opto-Cofilin the excitation of mCherry (555 nm) was combined with 488 nm irradiation at 1% laser power and a pixel dwell of 2.06 µsec.

Image processing and quantification of nuclear volumes, chromatin densities and 3D fluorescence intensities

Image processing was performed with IMARIS (Bitplane), FIJI (NIH) and Photoshop CS6 (Adobe).

For quantification of nuclear volume in living NIH3T3 cells, images were acquired every 2.5 or 5 min over an interval of 90 min. Complete z-stacks of the signal obtained by either H2B-mCherry (Fig. 3c, d, f, g) or SiR-DNA (Fig. 6k; Supp. Fig. 3a, b) were analyzed with IMARIS. 3D surfaces based on the nuclear-specific signal were generated, and their respective volumes were measured over time. Chromatin density was calculated by dividing the sum of H2B or SiR-DNA fluorescence intensities by total nuclear volume.

For measuring nuclear fluorescence intensities in 3D, a nuclear staining (i.e. DAPI) was used to threshold a nuclear region of interest (with FIJI for 2D data, and IMARIS for 3D data), from which the respective pixel intensities were calculated.

PALM and measurement of nuclear actin filament width

For super-resolution imaging of nAC-Dendra2, NIH3T3 cells were washed and fixed in 3.7 % formaldehyde (FA), 20 min at room temperature. For all super-resolution imaging, a 1:5000 dilution of fluorescent beads (TetraSpeck™ Microspheres, 0.1 µm, Life Sciences T7279 or FluoSpheres 715/755, Life Sciences F8799) was sonicated to break up clumps of beads. ~5 µL of the beads were added to the sample and allowed to settle and adhere for 15 minutes, to serve as fiducial markers for drift correction. Super-resolution imaging was performed as described in detail elsewhere [30]. Briefly, a customized and automated Nikon Eclipse Ti microscope was equipped with 405 nm, 488 nm, 561 and 640 nm lasers (all OBIS, Coherent Inc.). Laser intensities were controlled by an acousto-optical tunable filter (Acal BFi Germany GmbH) to illuminate the sample using the quad color dichroic zt405/488/561/640rpc. The illumination could be switched from epifluorescence to total internal reflection fluorescence (TIRF) mode by a motorized TIRF mirror (Thorlabs, Germany). Fluorescence signals were collected by a quad line laser rejection filter ZET405/488/561/640 and the bandpass filters

ET 525/50, ET 610/75 or HC 689/23 dependent on the imaging channel (all filters AHF, Germany). The detection of the single fluorophore emissions was performed using an electron multiplying charged coupled device (emCCD iXon 888, Andor).

For PALM imaging of Dendra2, the sample was irradiated by about 1-2 kW/cm² (561 nm) and < 0.5 kW/cm² (405 nm) and imaged at an acquisition frame rate of 60 ms. Cells were imaged until all Dendra2 fluorophores were read-out. For STORM imaging of Phalloidin-Alexa 647, the sample was imaged in 100 mM Methyl diethanolamine (MEA) with a glucose oxidase oxygen scavenger system [31] illuminated with about 2-4 kW/cm^2 (640 nm) and recorded at an acquisition frame rate of 70 ms.

Super-resolution movies were analyzed by the RapidSTORM software [32] and post-processed by customized scripts written in Python programming language (Python Software Foundation, https://www.python.org/) to correct for sample drift during the image acquisition. From the post-processed data, the experimental Nearest Neighbor Approach (NeNA) resolution [33] was calculated and super-resolution images were reconstructed according to their individual resolution.

Filament widths were analyzed by a self-written, customized script for the FIJI software [34]. Briefly, the filaments were selected by a segmented line profile covering the filament width and length. To minimize the selection and pixelation error, selections were shifted by 0.5 pixels (5 nm) in all directions to obtain five measures in total for each filament. These selected ROIs were straightened to remove the individual curvatures of the filaments and projected along their long axis. The obtained profiles were fitted by a Gaussian which yields the filament widths by its FWHM-value. The optimal histogram bin size was calculated using the Freedman – Diaconis rule [35].

Fluorescent lifetime imaging microscopy (FLIM) of fluorescence resonance energy transfer (FRET)

For FLIM/FRET, NIH3T3 cells were transduced with lentiviruses encoding PGK-H2B-mCherry and PGK-GFP-H2B, and sorted for homogeneous expression. For experiments involving expression of Exportin 6, cells were seeded and synchronized by a single thymidine block, 24 hours after transfection of Flag-Exportin 6. After this, cells were washed 3x in PBS and cultured in normal media for 10 hrs. Cells were then fixed (2% PFA in PBS, 10 min), permeabilised (0.1% Triton in PBS, 10 min), and blocked (2% BSA in PBS, 30 min), before incubation with anti-Flag antibodies for 2 hours. Cells were washed 3x in PBS, and incubated with secondary Alexa Fluor 405-conjugated antibodies for 45 minutes. Cells were then washed again in PBS. Post-mitotic, Flag-Exportin 6-overexpressing cells were identified using 405 nm excitation.

In the case of Flag-WT/R62D mutant actin, transfected cells expressing Flag-WT/R62D-NLS-actin were sorted through SNAP-mediated tagging. Following this, cells were transduced to express GFP-H2B and mCherry-H2B, and sorted by FACS. For these experiments, cells were synchronised at G1/S transition using thymidine (2 mM for 20 hours). Cells were then washed three times in PBS, and returned to normal media containing 500 ng/ml Doxycycline to induce expression of Flag-actin derivatives. After 4 hours, 1 µM of CDK1i (RO-3306, Sigma) was added to the medium for a subsequent period of 4 hours. Cells were washed three times in PBS, and then returned to normal media containing 500 ng/ml Doxycycline. 30 min later, mitotic cells were isolated by mitotic shake off, centrifuged at 1500 x g for 5 min and plated onto PLL-coated 35 mm dishes. After one hour cells were pre-extracted with CSK buffer for 5 minutes, washed three times in PBS and fixed with 2% PFA.

Lifetime measurements were taken on a Leica TCS SP8 system, using a white light laser with a repetition rate of 20 MHz and an excitation wavelength of 488 nm. GFP-H2B emission was detected over an emission range of 495 – 530 nm. Data was fitted using FLIMfit software[36]. Temporal binning of the fluorescence decays was performed prior to fitting, resulting in 256 time bins per decay. Tail-fitting of the fluorescence images was performed pixel-wise with a single exponential model on all pixels above an intensity threshold of 175 photons, allowing spatial variations in fluorescence lifetime to be visualized.

Nuclear F-actin pulldown at mitotic exit

For nuclear F-actin pulldowns, RPE-1 cells were mitotically blocked by nocodazole (100 nM for 24 hours), before washout with growth medium. 4 hours after washout, cells were lysed and subjected to subcellular fractionation as described previously [8]. Purity of subcellular fractionations was controlled by immunoblotting for α-Tubulin and histone H3. The obtained nuclear lysates were incubated with 5 µg biotin-phalloidin at 4 °C and constant rotation for 2 hours. Then, pre-washed magnetic streptavidin dynabeads (Thermo Fisher) were added, following incubation at 4 °C and constant rotation for 2 hours. After washing, the magnetic beads were collected and boiled in 2x Laemmli buffer for 10 min. The supernatant containing lysed nuclear F-actin and associated proteins was used for further analyses.

Mass spectrometry-based protein identification

Samples were loaded on an SDS gel and immediately after they had entered the separation gel, electrophoresis was stopped and the protein bands were excised and subjected to in-gel digest using trypsin [37].

For mass spectrometric analysis an Orbitrap Velos Pro mass spectrometer (ThermoScientific) was used which was connected online with an Ultimate nanoRSLC-HPLC system (Dionex), equipped with a nano C18 RP column. 10 µL of the tryptic digest were usually injected onto a C18 pre-concentration column and automated trapping and desalting of the sample was performed at a flowrate of 6 µL/min using water/0.05% formic acid as solvent.

Tryptic peptides were separated with water/0.045% formic acid (solvent A) and 80% acetonitrile/0.05% formic acid (solvent B) at a flow rate of 300 nl/min: holding 4% B for five minutes, followed by a linear gradient to 45% B within 30 minutes and linear increase to 95% solvent B for 5 minutes. The column was connected to a stainless steel nanoemitter (Proxeon, Denmark) and the eluent sprayed directly towards the heated capillary of the mass spectrometer using a potential of 2300 V. A survey scan with a resolution of 60000 within the Orbitrap mass analyzer was combined with at least three data-dependent MS/MS scans with dynamic exclusion for 30 s either using CID with the linear ion-trap or using HCD and Orbitrap detection at a resolution of 7500.

Data analysis was performed using Proteome Discoverer (v4.0; ThermoScientific) with SEQUEST and MASCOT (v2.4; Matrix science) search engines using either SwissProt or NCBI databases.

Mitotic shake-off

For indicated immunoblot analyses, immunofluorescence staining and MNase assays, cells were seeded at 40% confluency and allowed to adhere for 8 hours. Cells were then serum starved for 24 hours, followed by addition of growth media, containing 0.33 µg/ml doxycycline for experiments involving dox-inducible protein expression. After 16 hours, nocodazole (100 nM) was added for 3 additional hours. Mitotic cells were collected by mitotic shake-off and washed three times in growth media. These mitotic cells were then reseeded and further processed for subsequent analyses.

Micrococcal nuclease (MNase) digestion assay

One million cells were harvested, and washed once with 1 ml of 1x RSB buffer (10 mM Tris, pH 7.6, 15 mM NaCl, and 1.5 mM $MgCl_2$). After centrifugation (3,000 x g), the cell pellet was resuspended in 1 ml of 1x RSB buffer with 1% Triton-X 100 and homogenized. Nuclei were collected by centrifugation (13,000 x g) and washed twice with 1 ml of buffer A (15 mM Tris, pH 7.5, 15 mM NaCl, 60 mM KCl, 0.34 M sucrose, and 0.1% β-mercaptoethanol, EDTA-free protease inhibitor cocktail). Nuclei were resuspended in 500 µl MNase reaction buffer (from NEB, 50 mM Tris-HCl, 5 mM $CaCl_2$ pH 7.9) and aliquoted into 100 µl aliquots. MNase digestion was performed in 100 µl reactions by addition of 50 Kunitz units of MNase (NEB) at 37 °C for 5 minutes. Reactions were terminated by adding 25 mM EDTA. DNA was purified using a PCR purification kit and 1000 ng of DNA was analyzed on a 1.5% agarose gel.

Animals

ICR mice were obtained from Kiwa Experimental Animals (Wakayama, Japan). This study conformed to the Guide for the Care and Use of Laboratory Animals. All animal experiments

were approved and performed under the guidelines of the Animal Research Committee of Kindai University.

***In vitro* fertilization of mouse oocytes and mRNA injection**

Female ICR mice (or ICR x ICR), aged 8-13 weeks, were superovulated with pregnant mare serum gonadotropin (PMSG; Novartis Animal Health, Japan), followed 48 hours later with human chorionic gonadotropin (hCG; ASKA Pharmaceutical). Cumulus–oocyte complexes were collected from the oviducts in HTF medium. The sperm suspension was added to the oocyte cultures, and morphologically normal fertilized oocytes were collected 1-1.5 hours after insemination at 37°C under 5% CO_2 in air. Fertilized oocytes were transferred to HEPES-CZB medium. mRNAs for nAC-GFP, actin^{R62D}-HA-NLS, actin^{wt}-HA-NLS, mCherry-Exportin 6, myc-GFP were injected using a piezo manipulator (Prime Tech). mRNAs were prepared from pCS2 [38] or pcDNA3.1 vectors [39]. In the case of pCS2 vectors, mRNAs produced from the SP6 promoter were subjected to the addition of polyA tails while pcDNA3.1 vectors were transcribed from the T7 promoter. Since the translation efficiency is different between mRNAs produced from pCS2 vectors and those from pcDNA3.1 vectors, different concentrations of mRNA were injected; nAC-GFP (150 ng/μl), HA-NLS-actin^{R62D} (650 ng/μl), HA-NLS-actin^{wt} (650 ng/μl), mCherry-Exportin 6 (1,000 ng/μl) and myc-GFP (1,000 ng/μl), histone H2B-mCherry (5 ng/μl). After mRNA injections, the fertilized embryos were cultured in KSOM medium at 37°C in a 5% CO2 atmosphere. mCherry-Exportin 6 mRNA or control myc-tagged GFP mRNA was injected into oocytes denuded by 0.1% hyaluronidase before subsequent *in vitro* fertilization.

Confocal microscopy of oocytes

mRNA-injected embryos were fixed in 4% formaldehyde for 10 min and washed three times in PBS containing 0.01% PVA. Then, fixed embryos were incubated in PBS-BSA with 0.2% Triton-X for 60 min, followed by three time washes with PBS-BSA. Washed embryos were stained with 5 µg/ml DAPI for 15 min, followed by three times washing using PBS-BSA. Embryos were mounted and observed under a confocal microscope (LSM800, ZEISS). Images were analyzed using the ZEN software (ZEISS).

Electron microscopy (EM)

For EM-based analysis of chromatin compaction at mitotic exit, NIH3T3 cells (either stably expressing BFP-NLS, NLS-BFP-actin^{R62D} or transfected with GFP-Exportin 6 or NLS-mCherry-Cofilin) were synchronised at G1/S transition using thymidine (2 mM for 20 h). Expression of GFP-Exportin 6 and NLS-mCherry-Cofilin was ensured by FACS-based cell sorting prior to sample preperation. Cells were washed three times in PBS, and then returned to normal media containing 500 ng/ml Doxycycline. After 4 hours, analysis of flow cytometry data, using the Watson (Pragmatic) model, determined that 40% of cells had completed S phase. This time point was therefore chosen to add 1 µM of CDK1i (RO-3306, Sigma), for a period of 4 hours. Cells were washed three times in PBS, and then returned to normal media containing 500 ng/ml Doxycycline. 30 min later, mitotic cells were isolated by mitotic shake off. Cells were centrifuged at 1500 x g for 5 min, and plated onto PLL-coated 35 mm dishes.

After 1 hour, cells were trypsinised and centrifuged at 1500 x g for 5 min. Pellets were re-suspended in complete media containing 10% BSA, and centrifuged at 1500 x g for 5 min. 1 µl of this cell pellet was then put into a 0.1 mm gold membrane carrier and high pressure frozen (Leica EM PACT2). Samples were then freeze-substituted in a freeze-substitution acetone mix, containing 0.1% uranyl acetate and 1% osmium tetroxide. During

this procedure, samples were first held at -90°C, then brought to 0°C, over a period of 18 hrs. These samples were then embedded in EPON, and baked at 60°C for 48 hrs. 70 nm sections were cut using an ultratome, which were stained with uranyl acetate and lead citrate and images were taken at 2900x magnification on a FEI Tecnai 12 TEM, operated at 120kV.

For analysis, nuclei and nucleoli were manually segmented in 2D slice images across the cell using the freehand selection tool of ImageJ/Fiji to generate a binary mask of the nucleoplasm. Condensed chromatin was then semi-automatically segmented across the nucleoplasmic region using the WEKA Trainable Segmentation plugin for ImageJ/Fiji [40]. Classification was based on the Gaussian blur, Sobel filter, Hessian, Difference of Gaussians and membrane projections metrics using the built-in fast random forest algorithm. Due to the variability in chromatin staining, it was necessary to train a new classification model for each image. Condensed chromatin distribution was subsequently analysed in the segmented images using a custom ImageJ/Fiji macro, which measured the total condensed chromatin area and perimeter, as well as the area fraction of condensed chromatin, as a proportion of the total nucleoplasmic area.

Atomic force microscopy

To obtain early G1 or interphase NIH3T3 nuclei, cells were collected 60 min or 7 hours after mitotic shake-off, respectively. Nuclei were isolated as described previously [41]. Atomic force microscopy measurements were conducted in aqueous solution utilizing a Multi-mode VIII microscope with Nanoscope V controller and a PeakForce feedback control mechanism with an enclosed liquid cell. Isolated live nuclei were bound to a poly-L-lysine coasted glass coverslip and remained hydrated in this buffer (20 mM HEPES at pH 7.8, 25 mM KCl, 5 mM

MgCl2, 0.25 M sucrose and 1 mM ATP) to increase the longevity of the nuclei for investigation. The surface morphologies of nuclei were observed to remain unchanged under these conditions, allowing multiple nuclei to be tested in each sample and an average surface roughness and associated error to be calculated for each nucleus type. Using SCANASYST-FLUID cantilevers [Bruker, CA, USA] of nominal spring constant 0.7 N/m and nominal tip radius 2 nm, the force applied to plane of the sample by the AFM tip was kept below 1 nN, thus imaging stability was maintained whilst avoiding tip-induced deformation of the sample. Images were collected at a scan rate of 0.404 Hz with at 500 x 500 pixels giving a digital resolution of ~10 nm/pixel. Nuclear height and roughness (Rq) were calculated and quantified for the corresponding nuclei. Surface roughness (Rq) was defined as root mean square average of height deviations.

Statistics and Reproducibility

For each experiment, sample sizes were chosen based on initial pilot experiments. Similar experiments reported in previous publications were further used to direct sample sizes. No data were excluded from the analysis. No blinding or randomization was used in the course of the experiments. All attempts of replication were successful. Statistical analyses were performed with Prism 7 (GraphPad). Data are presented as stated in the respective figure legends. All *t*-tests were performed as unpaired, two-sided *t*-tests.

Data availability

Mass spectrometry data have been deposited in ProteomeXchange with the primary accession code PXD213854. Datasets generated and analysed during the current study are available from the corresponding author on reasonable request.

335

336

337 **References**

338 28. Meerbrey, K. L. *et al.* The pINDUCER lentiviral toolkit for inducible RNA interference in
339 vitro and in vivo. *Proc. Natl. Acad. Sci. U. S. A.* **108,** 3665–3670 (2011).

340 29. Grikscheit, K., Frank, T., Wang, Y. & Grosse, R. Junctional actin assembly is mediated
341 by Formin-like 2 downstream of Rac1. *J. Cell Biol.* **209,** 367–376 (2015).

342 30. Endesfelder, U. & Heilemann, M. Direct stochastic optical reconstruction microscopy
343 (dSTORM). *Methods Mol. Biol.* **1251,** 263–76 (2015).

344 31. van de Linde, S. *et al.* Direct stochastic optical reconstruction microscopy with
345 standard fluorescent probes. *Nat. Protoc.* **6,** 991–1009 (2011).

346 32. Wolter, S. *et al.* rapidSTORM: accurate, fast open-source software for localization
347 microscopy. *Nat. Methods* **9,** 1040–1 (2012).

348 33. Endesfelder, U., Malkusch, S., Fricke, F. & Heilemann, M. A simple method to
349 estimate the average localization precision of a single-molecule localization
350 microscopy experiment. *Histochem. Cell Biol.* **141,** 629–38 (2014).

351 34. Schindelin, J. *et al.* Fiji: an open-source platform for biological-image analysis. *Nat.*
352 *Methods* **9,** 676–82 (2012).

353 35. Freedman, D. & Diaconis, P. On the histogram as a density estimator:L 2 theory.
354 *Zeitschrift für Wahrscheinlichkeitstheorie und Verwandte Gebiete* **57,** 453–476 (1981).

355 36. Warren, S. C. *et al.* Rapid Global Fitting of Large Fluorescence Lifetime Imaging
356 Microscopy Datasets. *PLoS One* **8,** e70687 (2013).

37. Hellman, U., Wernstedt, C., Góñez, J. & Heldin, C. H. Improvement of an "In-Gel" digestion procedure for the micropreparation of internal protein fragments for amino acid sequencing. *Anal. Biochem.* **224,** 451–5 (1995).

38. Miyamoto, K., Pasque, V., Jullien, J. & Gurdon, J. B. Nuclear actin polymerization is required for transcriptional reprogramming of Oct4 by oocytes. *Genes Dev.* **25,** 946–58 (2011).

39. Yamagata, K. & Ueda, J. Long-term live-cell imaging of mammalian preimplantation development and derivation process of pluripotent stem cells from the embryos. *Dev. Growth Differ.* **55,** 378–389 (2013).

40. Arganda-Carreras, I. *et al.* Trainable_Segmentation: Release v3.1.2. (2016). doi:10.5281/ZENODO.59290

41. Guilluy, C. *et al.* Isolated nuclei adapt to force and reveal a mechanotransduction pathway in the nucleus. *Nat. Cell Biol.* **16,** 376–381 (2014).

Supplementary Information

1. Supplementary Figures

Supplementary Figure 1 | Nuclear actin levels during mitotic exit are not affected by expression of nAC-GFP. Nuclear actin filaments are a conserved feature among different mammalian cell lines and form independent of Emerin, Lamin A/C, and the LINC complex. **(a)** 3D nuclear fluorescence intensities (FI) of stably expressed mCherry-actin were measured at indicated times after cell division (0 min corresponds to anaphase) to compare its nuclear distribution in the absence or presence of co-expressed nAC-GFP. Nuclei were counterstained with SiR-DNA. Data are shown as mean ± SD (n=13 mitotic events per condition, pooled from several independent experiments). **(b)** NIH3T3 cells stably expressing mCherry-actin were transfected with GFP-Exportin 6 and followed during the time-course of mitotic cell division. Images show single confocal slices to illustrate nuclear distribution of mCherry-actin in postmitotic cells in either the presence (indicated by asterisks) or absence (arrowheads) of GFP-Exportin 6. Note the nuclear fluorescence signal produced by mCherry-actin in control daughter nuclei (indicated by arrowheads). The experiment was performed once. Time stamp, hours:min; scale bar, 10 µm. **(c)** Time-lapse imaging of stably nAC-GFP (green) expressing MCF10A, HT1080, and RPE-1 during cell division reveals nuclear F-actin formation at mitotic exit. Images show maximum intensity projections. Scale bar, 10 µm; time stamp, min:sec. **(d, e)** Quantification of incidence **(d)** and duration **(e)** of nuclear F-actin formation during mitotic exit in MCF10A, HT1080, and RPE-1 cells stably expressing nAC-GFP. Data are shown as mean + SEM (n=40 (MCF10A, HT1080), n=30 (RPE-1) mitotic events, pooled from several independent experiments). **(f, g)** Quantification of the incidence **(f)** and duration **(g)** of nuclear F-actin formation during

mitotic exit in nAC-GFP expressing NIH3T3 cells, treated with indicated siRNAs. Data are shown as mean + SD (n=30 cells per condition, pooled from 2 independent experiments). **(h)** Immunoblot validating efficient siRNA-mediated knockdown of Lamin A/C and Emerin. The experiment was performed once. **(i)** Time-lapse imaging of NIH3T3 cells expressing nAC-GFP (grey) together with tagRFP-KASH (red, insets) to disrupt the LINC complex during and after mitotic division. The experiment was performed once. Scale bar, 10 μm; time stamp, min:sec. Unprocessed original scans of blots are shown in Supplementary Fig. 7.

Supplementary Figure 2 | Super-resolution imaging of nuclear F-actin at mitotic exit.

(a) PALM images of NIH3T3 cells stably expressing nAC-Dendra2 (orange) at mitotic exit used to calculate filament widths in Fig. 2b. Experimental resolutions after drift correction (see Methods) are 38 ± 1 nm (1, 2, 4), 39 ± 1 nm (3), 33 ± 1 nm (5, 6), 35 ± 1 nm (7,8). Cells 5 and 6 are shown in Fig. 2a. Scale bars, 5 μm. **(b)** Filaments were analysed by a self-written, customized script for FIJI. First, ROIs were drawn along filaments (I). To minimize the selection and pixelation error, selections were shifted by 0.5 pixels (5 nm) in all directions to obtain five measures in total for each filament by straightening all selections (II). To determine the filament width, lengthwise intensity profiles of the five filament selections were fitted with Gaussians (III). The average full width at half maximum (FWHM) of the five selections yields the average filament width. Scale bar, 0.5 μm. **(c)** Mitotic cell division of native NIH3T3 cells was monitored over time using DIC (Differential interference contrast) to allow for formaldehyde fixation at defined time points after anaphase, as indicated. Stochastic Optical Reconstruction Microscopy (STORM) images focus on the corresponding nuclei labelled by phalloidin (see Methods for details). The dashed rectangle is shown

magnified in Fig. 2c. Experimental resolutions after drift correction are 40 ± 1 nm (15 min**,** 45 min-cell 1), 30 ± 1 nm (45 min-cell 2) and 34 ± 1 nm (60 min). Scale bars, 5 µm.

Supplementary Figure 3 | Actin dynamics but not transcriptional inhibition affect early G1 nuclear expansion. Detection of Flag-actin derivatives by doxycycline-inducible T2A-SNAP fusions.

(a) 3D surface reconstructions of NIH3T3 nuclei (vizualized by SiR-DNA) at indicated times after drug treatment at mitotic exit. Scale bar, 10 µm; time stamp, hours:min. **(b)** Nuclear volume quantifications in cells treated similar to **a**. Data is shown as mean ± SD (n=50 nuclei per condition, pooled from at least 3 independent experiments). **(c)** Design of Flag-tagged nuclear actin derivatives linked to the SNAP-tag by a T2A peptide. Upon translation, the T2A peptide is cleaved resulting in equimolar expression of Flag-NLS-actin and the SNAP-tag. Accordingly, labelling of the SNAP-tag allows for indirect detection of Flag-NLS-actin in living cells. **(d)** Immunoblot confirms doxycycline-induced expression of Flag-NLS-actin-T2A-SNAP derivatives. A single band indicates efficient cleavage of Flag-NLS-actin-T2A-SNAP. **(e)** Confocal images of fixed NIH3T3 cells expressing nAC-GFP transfected with Flag-NLS-actin-T2A-SNAP derivatives. In contrast to Flag-NLS-actin the SNAP-tag (labelled by SiR-647) displays pancellular distribution. Scale bar, 10 µm. **(f)** Confocal images of fixed NIH3T3 cells at mitotic exit show expression of Flag-NLS-actin-T2A-SNAP derivatives, as indicated. Magnifications correspond to dashed rectangles and highlight Flag-actin. Scale bar, 10 µm. **(g)** Nuclear volume quantifications in live NIH3T3 cells stably expressing H2B-mCherry and doxycycline-induced BFP-NLS, NLS-BFP-actin^{R62D} or Flag-NLS-actin-T2A-SNAP derivatives. Expression of the indicated constructs was induced during G_0. Data are mean + SD from n=30 nuclei per condition. **(h)** RT-qPCR analysis of *FOS* expression in serum-starved NIH3T3

cells, pre-treated with Flavopiridol (1 µM for indicated times) before stimulation with serum (20% FCS, fetal calf serum) for 30 minutes. Note that 15 min pre-treatment with Flavopiridol efficiently inhibits serum-induced transcriptional upregulation of *FOS* mRNA. Data are shown as mean from n=2 independent experiments. **(i)** Nuclear volume analysis in NIH3T3 cells stably expressing H2B-mCherry in the presence of Flavopiridol (1 µM) or DMSO (0.1%). Flavopiridol was added at metaphase prior to imaging the subsequent expansion of daughter nuclei. Data are shown as mean ± SD (n>14 nuclei [precise n?] per condition, pooled from 3 independent experiments). Unprocessed original scans of blots are shown in Supplementary Fig. 7.

Supplementary Figure 4 | Inhibition of nuclear F-actin formation impairs chromatin decompaction at mitotic exit

(a) Quantification of GFP-H2B fluorescence lifetime in cells expressing GFP-H2B alone, or in combination with mCherry-H2B and indicated treatments: trichostatin A (TSA), or sodium azide (NaN3) together with 2-deoxyglucose (2-DG). $^{**}P < 0.01$, $^{***}P < 0.001$ calculated by one-way ANOVA. **(b)** Quantification of fluorescence lifetime reveals no significant difference in GFP fluorescence lifetime upon expression of and staining for Flag-Exportin 6 using a Alexa Fluor 405-conjugated antibodies. ns, non-significant in one-way ANOVA. **(c)** Comparative immunoblot analysis of histone modifications (H3S10ph, H4K16ac) in NIH3T3 cells induced to express BFP-NLS or NLS-BFP-actin^{R62D} and undergoing either asynchronous (asyn.) or synchronized (mitotic shake off) culture, as indicated. **(d, e)** Images and quantitative immunofluorescence analysis of nuclear Aurora B **(d)** and KAT5 **(e)** (both green; nuclei are stained with DAPI (magenta)) in NIH3T3 cells at mitotic exit expressing Flag-NLS-actin-T2A-SNAP derivatives, as indicated. Data are shown as mean ± SD (n=20 nuclei per

condition, pooled from three independent experiments). Scale bar, 10 µm. ****$P < 0.0001$ calculated by *t*-test. **(f)** Analysis of chromatin compaction by an MNase accessibility assay 45 min after mitotic shake-off in NIH3T3 cells expressing either doxycycline-induced Flag-NLS-actin^{wt} or -actin^{R62D}. Graph shows quantified pixel intensities corresponding to band intensities. **(g)** Example images illustrating the pipeline used for the quantification of condensed chromatin in cryo-electron microscopy images (for details see Methods). Based on raw images (I) nuclei and nucleoli were manually segmented (II). Condensed chromatin was semi-automatically segmented across the nucleoplasmic region and classified (III) allowing for an assessment of its distribution using a custom ImageJ/Fiji macro (IV). **(h)** Representative electron microscopy images of cryo-preserved, synchronized early G_1 NIH3T3 cells expressing GFP-Exportin 6 corresponding to Figure 4l. Scale bar, 2 µm. Unprocessed original scans of blots are shown in Supplementary Fig. 7. Immunoblot in c and MNase accessibility assay in f represent 1 out of 2 independent experiments.

Supplementary Figure 5 | Inhibition of nuclear F-actin formation impairs Pol II-dependent transcription and preimplantation development of mouse embryos.

(a) Images corresponding to Figure 5a showing RNA Pol II pS5 stainings (grey) in NIH3T3 cells expressing either GFP or GFP-Exportin 6 at indicated times after mitotic shake-off. Scale bar, 5 µm. **(b)** Images corresponding to Figure 5g showing preimplantation development of mouse embryos expressing either mCherry-Exportin 6 or myc-tagged GFP as a control. Similar amounts of mRNA were injected into oocytes at the metaphase II stage, followed by *in vitro* fertilization. Scale bar, 100 µm.

Supplementary Figure 6 | P-Cofilin levels change during mitotic exit and nuclear Cofilin-1 is essential for filament disassembly during mitotic exit.

(a) Representative immunostaining of p-Cofilin (grey, DAPI (blue)) in NIH3T3 cells treated with si-Control or si-Cofilin to validate specificity of the obtained fluorescence signals. Asterisks indicate presumably non-silenced cells. Scale bar, 10 µm. The experiment was performed once. **(b)** Images corresponding to quantifications shown in Figure 6e. Confocal images show single slices at indicated time points after mitotic shake-off. Scale bar, 5 µm. **(c)** Immunoblot detecting p-Cofilin and Cofilin in RPE-1 cells after washout of nocodazole. Decreasing H3S10ph levels proof for successful release from the nocodazole-induced mitotic block. **(d)** P-Cofilin/Cofilin ratio was calculated by densitometric quantification of immunoblot intensities. Data are shown as mean + SD from n=3 independent experiments. **(e)** Time-lapse imaging of NIH3T3 cells during mitotic exit corresponding to Figure 6j. Cells stably express nAC-GFP (green) together with either WT- or NES-mCherry-Cofilin (red) and were treated with siRNA against the 3'-UTR of endogenous Cofilin-1. Scale bar, 10 µm. **(f)** Stably nAC-GFP expressing NIH3T3 cells were transfected with NLS-mCherry-Cofilin and followed during mitotic exit. Images show maximum intensity projections of confocal z-stacks and illustrate the absence of nuclear F-actin formation which was observed in 10 of 12 mitotic events. Time, hours:min; scale bar, 10 µm. **(g)** Immunoblot validating expression of opto-Cofilin in cells treated with either control siRNA or siRNA directed against the 3'-UTR of endogenous Cofilin-1. Unprocessed original scans of blots are shown in Supplementary Fig. 7.

Supplementary Figure 7 | Unprocessed original scans of Western blot analysis

2. Supplementary Tables

Supplementary Table 1

Table illustrating the incidence and duration of nuclear F-actin formation at mitotic exit upon siRNA-mediated knockdown of actin nucleators or regulators. All siRNA sequences used showed greater than 50% knockdown efficiency on mRNA level for the intended target, as determined by RT-qPCR (compared to control siRNA and normalized to expression of TBP). Statistical analysis did not show a significant difference for any condition compared to control cells, as determined by one-way ANOVA. n.d., not determined. Data are shown as mean +/- SEM, pooled from at least 2 independent experiments. Sample sizes (number of mitotic events) for each condition are shown within the table.

Supplementary Table 2

Table summarizing the results of nuclear F-actin pulldown, as well as a control pulldown (without biotin-phalloidin), performed at mitotic exit and analysed by mass spectrometry (see Methods for details).

Supplementary Table 3

Table listing the information of antibodies used in this study.

3. Supplementary Videos

Supplementary Video 1 | Transient nuclear F-actin formation can be detected during mitotic exit.

Video corresponding to Fig. 1a shows transient formation of nuclear F-actin during and after cell division in NIH3T3 cells as visualized by nAC-GFP (green). In addition, cells express LifeAct-mCherry (red). Scale bar, 10 µm.

Supplementary Video 2 | Nuclear F-actin shows dynamic turnover in cells at mitotic exit.

Video corresponding to Fig. 1b shows dynamic reorganization of actin filaments after mitotic division in NIH3T3 cells as visualized by nAC-GFP (green). In addition, cells express Lamin-nanobody-SNAP, labelled by a SiR-647 dye (LaminCB-SNAP|SiR-647, magenta). Scale bar, 10 µm.

Supplementary Video 3 | Nuclear F-actin forms within interchromatin spaces.

Video corresponding to Fig. 4a shows dynamic reorganization of actin filaments after mitotic division in NIH3T3 cells as visualized by sAC-GFP (green). In addition, cells express H2B-mCherry (red) to visualize chromatin content. Scale bar, 10 µm; time stamp, h:min:s.

Supplementary Video 4 | Nuclear actin filaments reshape newly assembled nuclei.

Video corresponding to Fig. 3a shows NIH3T3 cells during mitotic exit, stably expressing nAC-GFP (green) and H2B-mCherry (red). Scale bar, 10 µm; time stamp, min:s.

Supplementary Video 5 | Knockdown of Cofilin affects nuclear actin dynamics during mitotic exit.

Video corresponding to Fig. 6f, g. Time-lapse imaging of NIH3T3 cells stably expressing nAC-GFP (green), treated with si-control or si-Cofilin during mitotic exit. Video shows three representative examples for each condition. Note the appearance of excessive and stable nuclear actin filaments in si-Cofilin-treated cells. Scale bar, 10 μm.

Supplementary Video 6 | Light-regulated control of opto-Cofilin subcellular localization.

Video corresponding to Fig. 7d shows NIH3T3 cells stably expressing opto-Cofilin (grey). Single confocal slices were acquired at 10 sec intervals, and cells were temporarily illuminated by additional blue laser light (488 nm, indicated by a green bar) to promote reversible nuclear export of opto-Cofilin.

Supplementary Video 7 | Formation of excessive, stable nuclear F-actin upon light-regulated nuclear exclusion of opto-Cofilin.

NIH3T3 cells stably expressing nAC-SNAP (labelled by SiR-647, grey) and opto-Cofilin (red) were treated with si-Cofilin (3'-UTR) and imaged during and after mitosis. Cells were imaged either with (+ light, lower panel) or without (- light, upper panel) additional blue laser light (488 nm) to promote sustained nuclear export of opto-Cofilin.

Supplementary Video 8 | Reversible formation of excessive, stable nuclear F-actin by light-controlled subcellular shuttling of opto-Cofilin.

Video corresponding to Fig. 7f shows NIH3T3 cells stably expressing nAC-SNAP (labelled by SiR-647, grey) and opto-Cofilin (red) during and after mitosis. Cells were treated with si-

Cofilin (3’-UTR) and temporarily illuminated by blue laser light (488 nm) to promote nuclear export of opto-Cofilin for a defined period of time (indicated by a green bar).

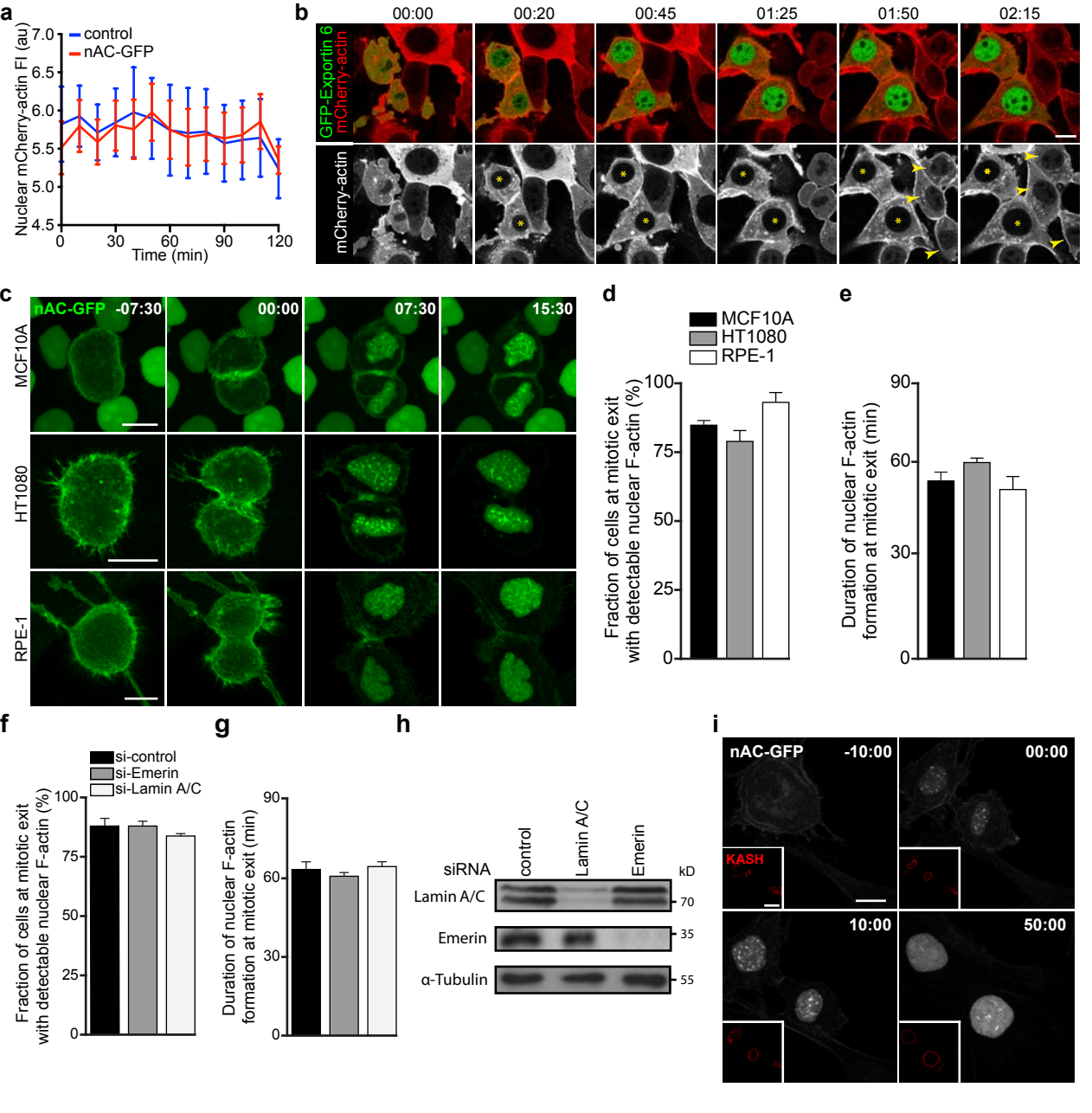
a
control
nAC-GFP
Nuclear mCherry-actin FI (au)
7.0
6.5
6.0
5.5
5.0
4.5
0
30
60
90
120
Time (min)
b
00:00
00:20
00:45
01:25
01:50
02:15
GFP-Exportin 6
mCherry-actin
mCherry-actin
c
nAC-GFP
-07:30
00:00
07:30
15:30
MCF10A
HT1080
RPE-1
d
MCF10A
HT1080
RPE-1
Fraction of cells at mitotic exit with detectable nuclear F-actin (%)
100
75
50
25
0
e
Duration of nuclear F-actin formation at mitotic exit (min)
90
60
30
0
f
si-control
si-Emerin
si-Lamin A/C
Fraction of cells at mitotic exit with detectable nuclear F-actin (%)
100
75
50
25
0
g
Duration of nuclear F-actin formation at mitotic exit (min)
90
60
30
0
h
siRNA
control
Lamin A/C
Emerin
kD
Lamin A/C
70
Emerin
35
α-Tubulin
55
i
nAC-GFP
-10:00
00:00
KASH
10:00
50:00

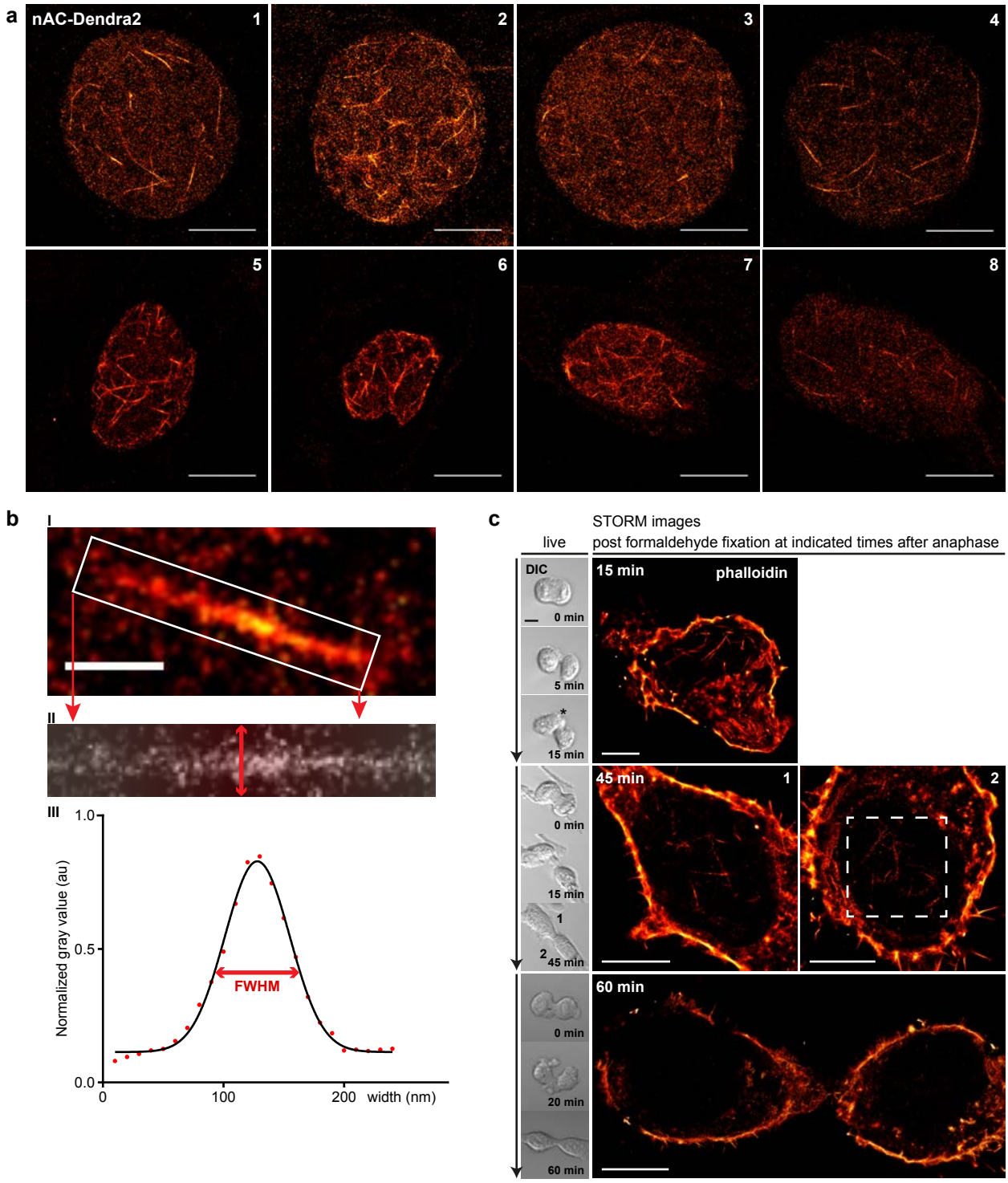
a
nAC-Dendra2
1
2
3
4
5
6
7
8
b
I
II
III
1.0
0.5
0.0
Normalized gray value (au)
FWHM
0
100
200
width (nm)
c
STORM images
live
post formaldehyde fixation at indicated times after anaphase
DIC
0 min
5 min
15 min
*
15 min
phalloidin
45 min
1
2
0 min
15 min
1
2
45 min
60 min
0 min
20 min
60 min

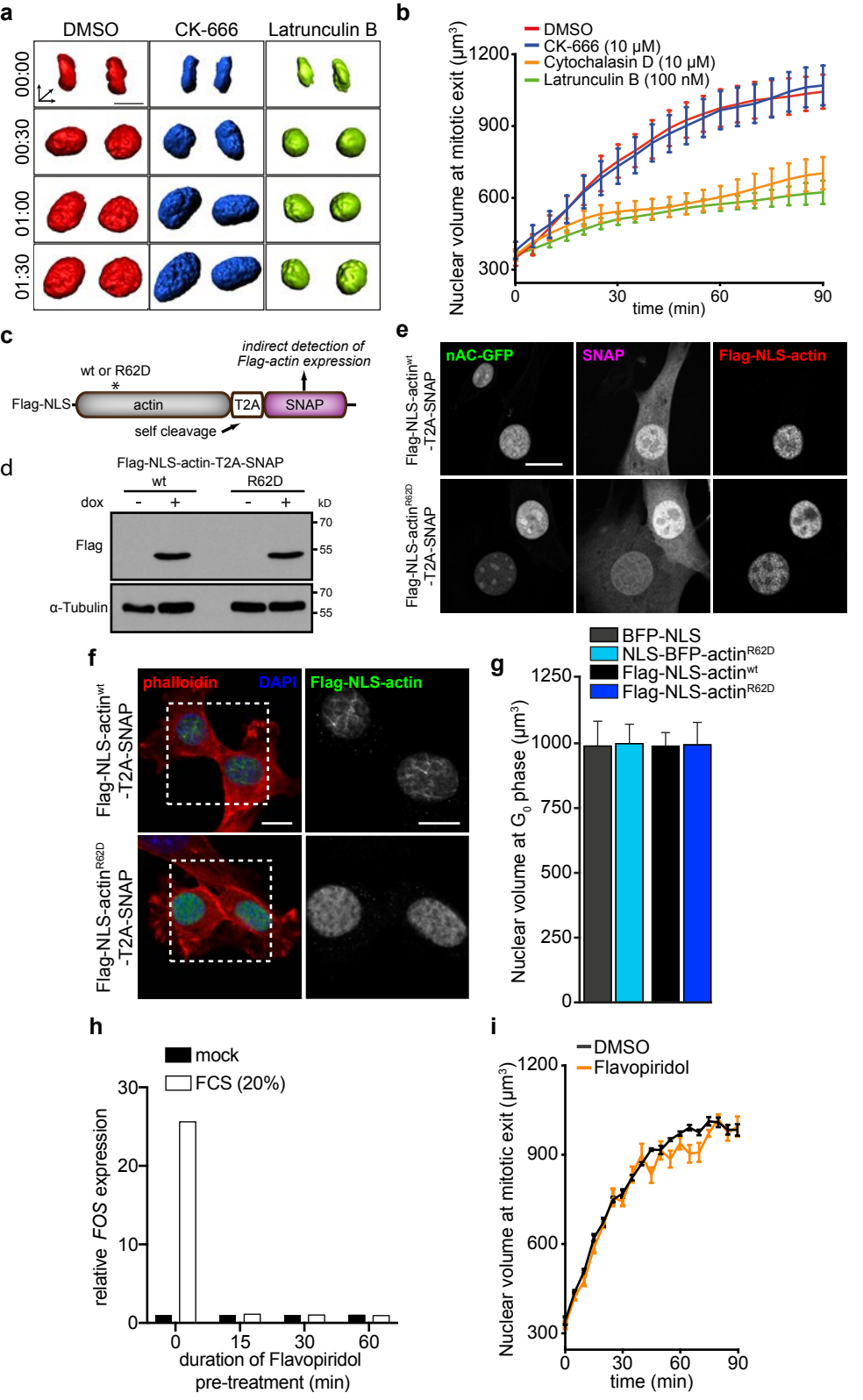
a
DMSO
CK-666
Latrunculin B
00:00
00:30
01:00
01:30
b
DMSO
CK-666 (10 µM)
Cytochalasin D (10 µM)
Latrunculin B (100 nM)
Nuclear volume at mitotic exit (µm³)
1200
900
600
300
0
30
60
90
time (min)
c
wt or R62D
*
Flag-NLS-
actin
T2A
SNAP
indirect detection of
Flag-actin expression
self cleavage
d
Flag-NLS-actin-T2A-SNAP
wt
R62D
dox
- + - +
kD
Flag
70
55
α-Tubulin
70
55
e
nAC-GFP
SNAP
Flag-NLS-actin
Flag-NLS-actinwt
-T2A-SNAP
Flag-NLS-actinR62D
-T2A-SNAP
f
phalloidin
DAPI
Flag-NLS-actin
Flag-NLS-actinwt
-T2A-SNAP
Flag-NLS-actinR62D
-T2A-SNAP
g
BFP-NLS
NLS-BFP-actinR62D
Flag-NLS-actinwt
Flag-NLS-actinR62D
Nuclear volume at G0 phase (µm³)
1250
1000
750
500
250
0
h
mock
FCS (20%)
relative FOS expression
30
20
10
0
0
15
30
60
duration of Flavopiridol
pre-treatment (min)
i
DMSO
Flavopiridol
Nuclear volume at mitotic exit (µm³)
1200
900
600
300
0
30
60
90
time (min)

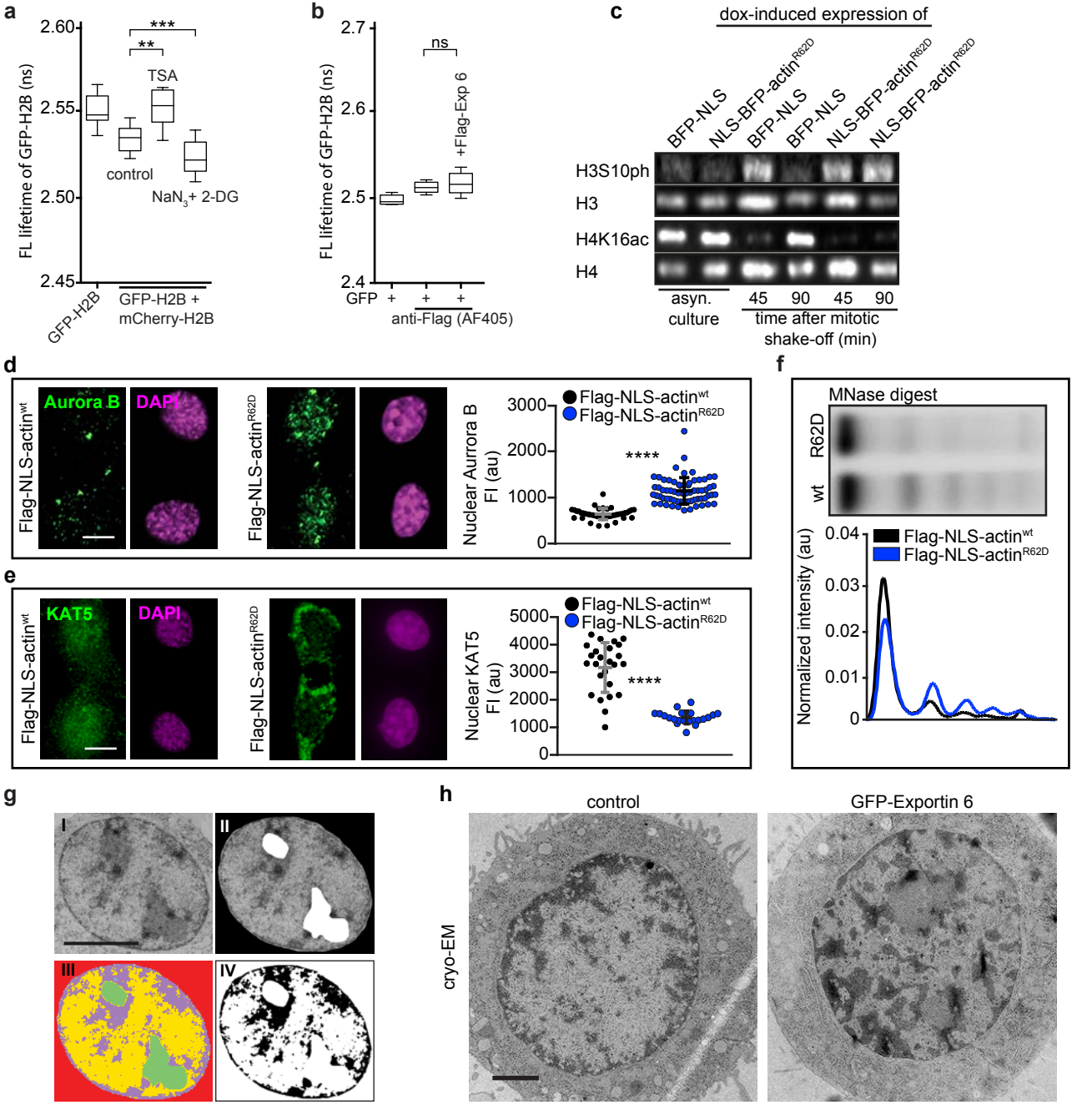
a
FL lifetime of GFP-H2B (ns)
2.60
2.55
2.50
2.45
***
**
TSA
control
NaN3+ 2-DG
GFP-H2B
GFP-H2B + mCherry-H2B
b
FL lifetime of GFP-H2B (ns)
2.7
2.6
2.5
2.4
ns
+Flag-Exp 6
GFP + + +
anti-Flag (AF405)
c
dox-induced expression of
BFP-NLS
NLS-BFP-actinR62D
BFP-NLS
BFP-NLS
NLS-BFP-actinR62D
NLS-BFP-actinR62D
H3S10ph
H3
H4K16ac
H4
asyn. culture
45 90 45 90
time after mitotic shake-off (min)
d
Flag-NLS-actinwt
Aurora B
DAPI
Flag-NLS-actinR62D
Nuclear Aurrora B FI (au)
3000
2000
1000
0
Flag-NLS-actinwt
Flag-NLS-actinR62D
****
e
Flag-NLS-actinwt
KAT5
DAPI
Flag-NLS-actinR62D
Nuclear KAT5 FI (au)
5000
4000
3000
2000
1000
0
Flag-NLS-actinwt
Flag-NLS-actinR62D
****
f
MNase digest
R62D
wt
Normalized intensity (au)
0.04
0.03
0.02
0.01
0
Flag-NLS-actinwt
Flag-NLS-actinR62D
g
I
II
III
IV
h
control
GFP-Exportin 6
cryo-EM

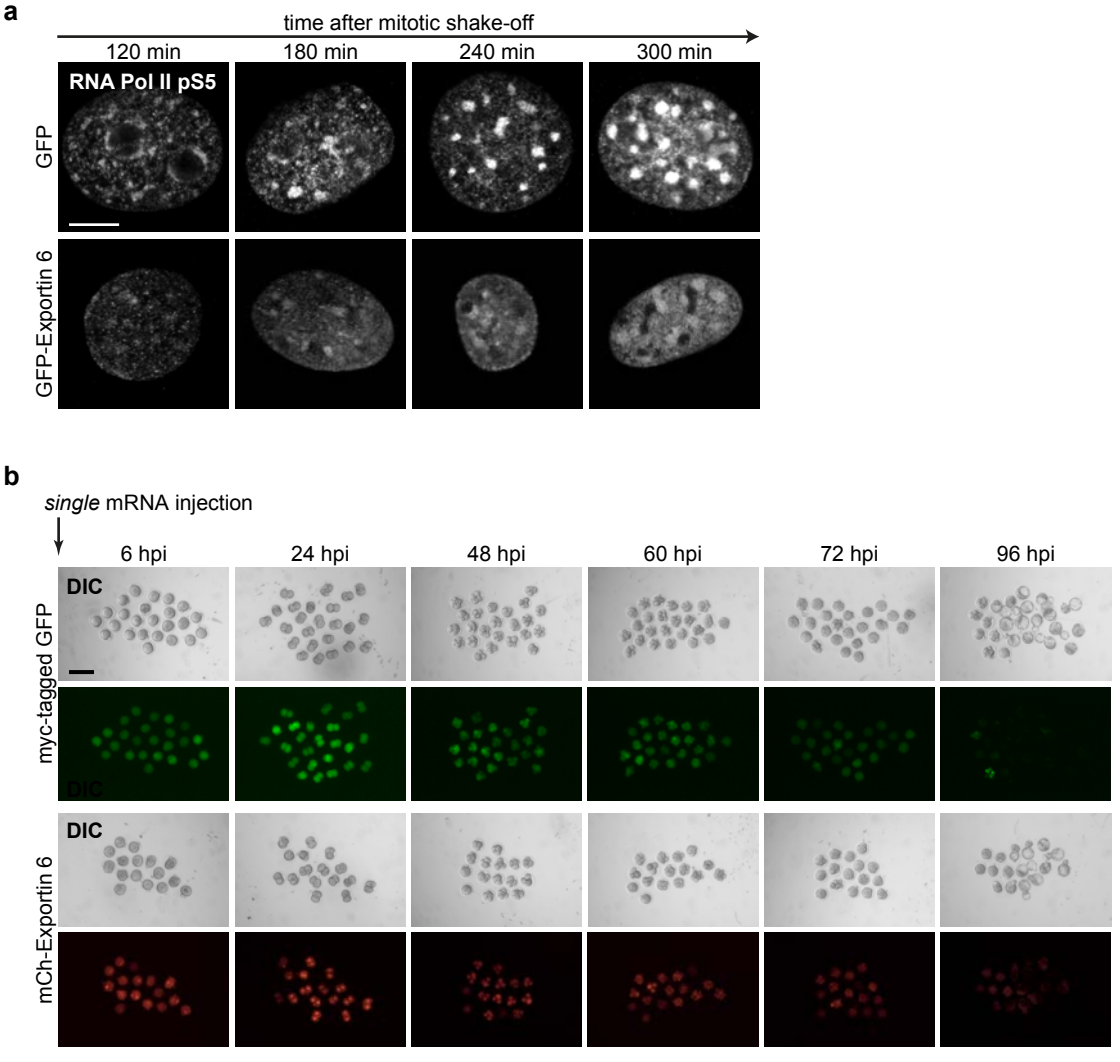
a
time after mitotic shake-off
120 min
180 min
240 min
300 min
RNA Pol II pS5
GFP
GFP-Exportin 6
b
single mRNA injection
6 hpi
24 hpi
48 hpi
60 hpi
72 hpi
96 hpi
DIC
myc-tagged GFP
DIC
mCh-Exportin 6

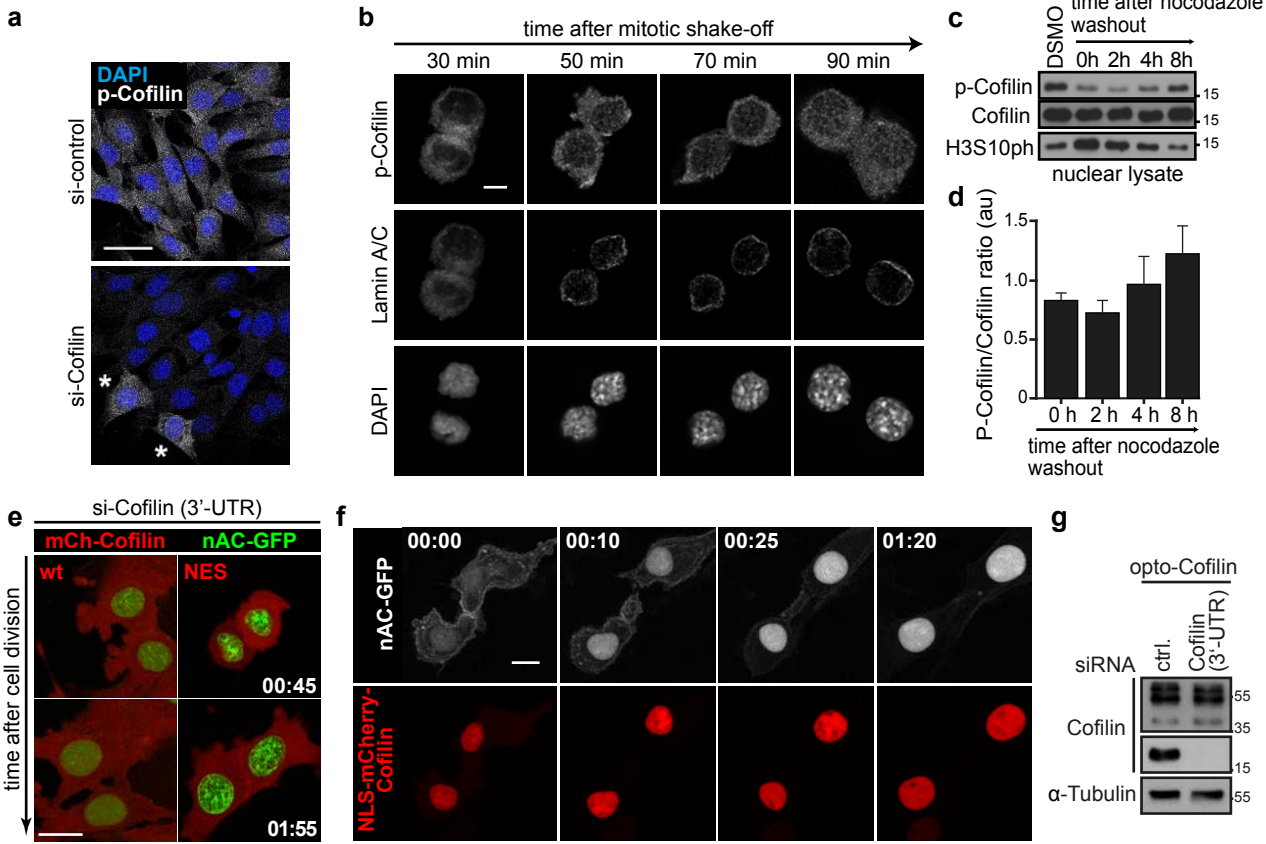
a
DAPI
p-Cofilin
si-control
si-Cofilin
*
*
b
time after mitotic shake-off
30 min
50 min
70 min
90 min
p-Cofilin
Lamin A/C
DAPI
c
DSMO
time after nocodazole washout
0h 2h 4h 8h
p-Cofilin
Cofilin
H3S10ph
15
15
15
nuclear lysate
d
P-Cofilin/Cofilin ratio (au)
1.5
1.0
0.5
0
0 h 2 h 4 h 8 h
time after nocodazole washout
e
si-Cofilin (3'-UTR)
mCh-Cofilin
nAC-GFP
wt
NES
00:45
01:55
time after cell division
f
00:00
00:10
00:25
01:20
nAC-GFP
NLS-mCherry-Cofilin
g
opto-Cofilin
siRNA
ctrl.
Cofilin (3'-UTR)
Cofilin
α-Tubulin
55
35
15
55

Figure 6g

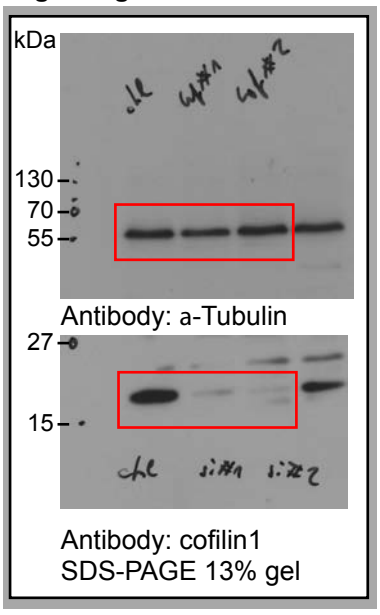

Suppl. Figure 3d

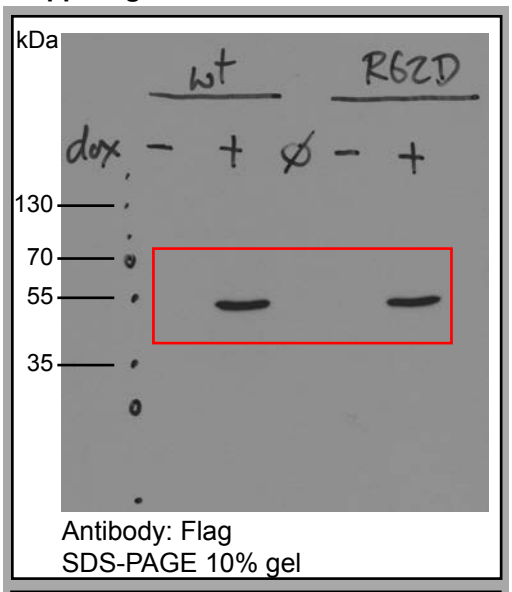

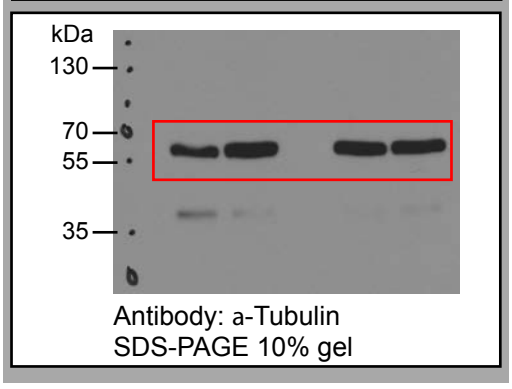

Figure 6i

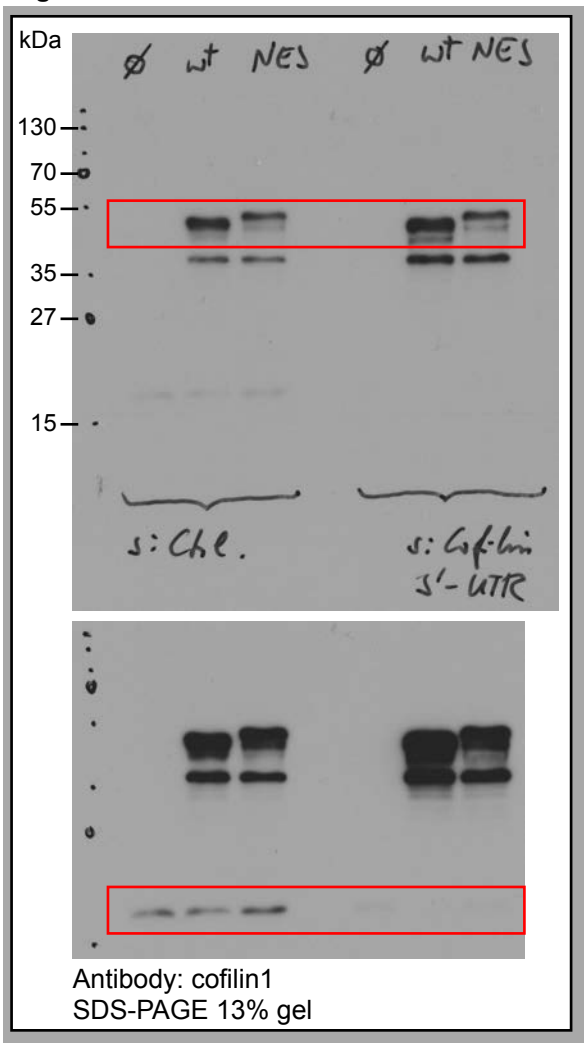

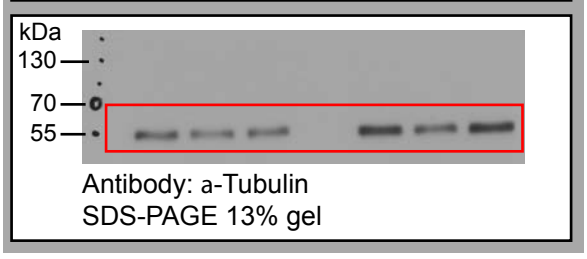

Suppl. Figure 6h

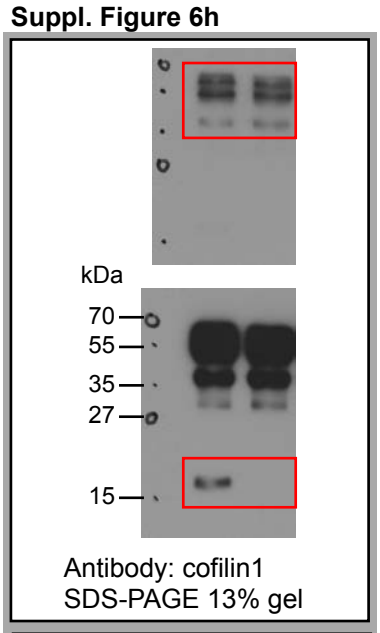

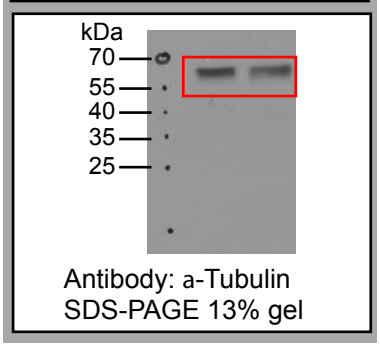

Suppl. Figure 6h

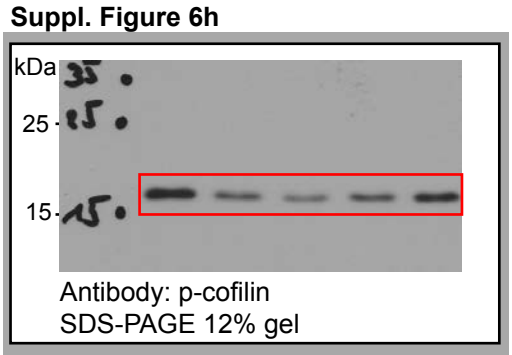

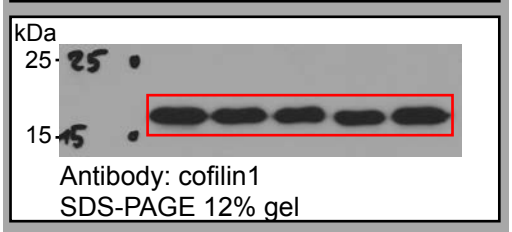

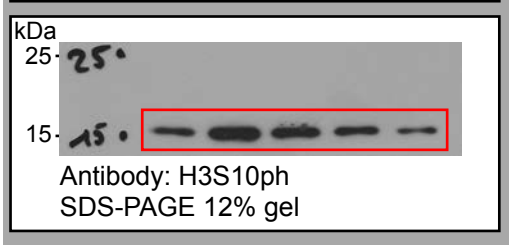

Suppl. Figure 4c

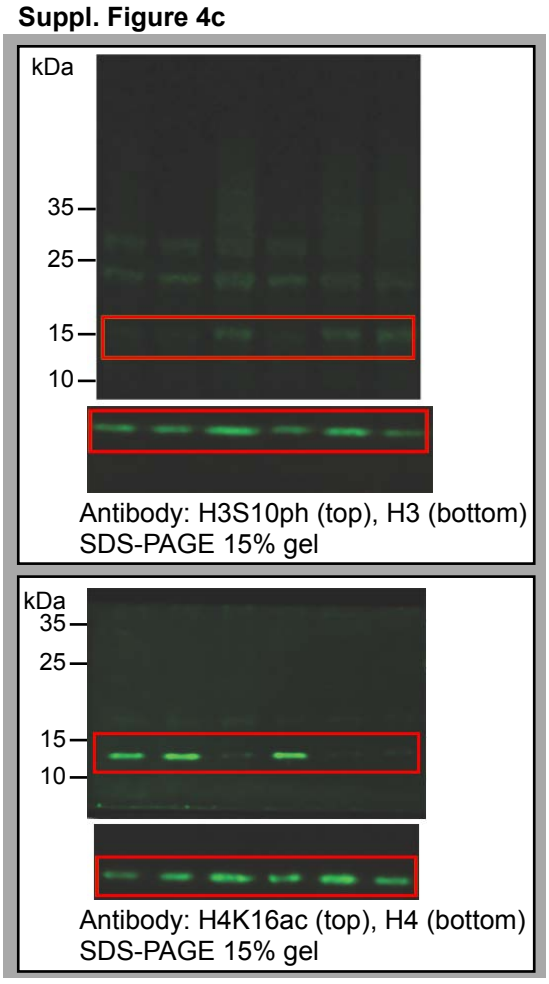

Figure 6b

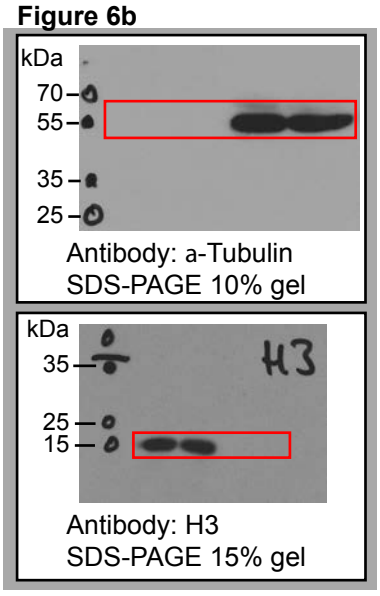

Suppl. Figure 1h

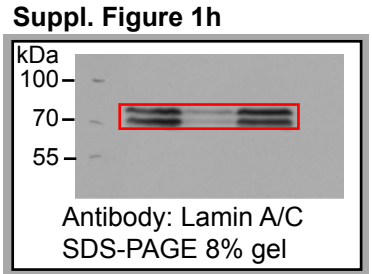

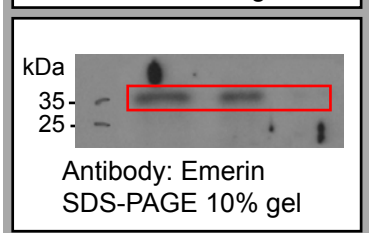

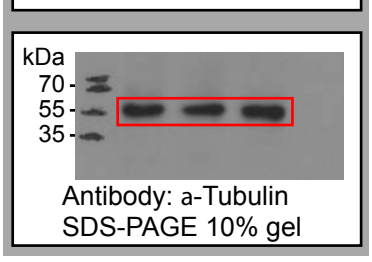

Figure 6c